Applied Energy 412 (2026) 127687

Contents lists available at ScienceDirect

Applied Energy

journal homepage: www.elsevier.com/locate/apen

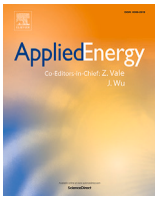

# Characterisation and performance evaluation of early-generation commercial sodium-ion batteries

Shiyun Liu [a,*], Kang Li [a,*], James Yu [b], Kailong Liu [c]

[a] School of Electronic and Electrical Engineering, University of Leeds, Leeds, LS2 9JT, UK
[b] SP Energy Networks, Glasgow, G2 5AD, UK
[c] School of Control Science and Engineering, Shandong University, Jinan, 250061, China

## HIGHLIGHTS

- Early-generation commercial Na-ion 18650 cells characterised against Li-ion.
- Na-ion retains measurable capacity at −40 °C where Li-ion fails.
- Cold operation amplifies cell-to-cell variability in commercial Na-ion cells.
- Low-temperature OCV hysteresis requires uncertainty-aware state estimation.
- Casing strain provides a viable state observable for layered-oxide chemistries.

## ARTICLE INFO

*Keywords:*
Sodium-ion battery
Cylindrical 18650 cell
Model parameterisation
Low-temperature operability
Casing strain
BMS control strategies

## ABSTRACT

Sodium-ion (Na-ion) batteries are a promising low-cost option for large-scale energy storage, yet practical deployment requires control-relevant characterisation of the commercial cells and their inherent variability. This work evaluates a population of early-generation 18650 layered-oxide $Na(Ni, Fe, Mn)O_2$ (NFM) cells from a monitoring, control, and model parameterisation perspective, benchmarking against $Na(Cu, Fe, Mn)O_2$ (CFM), polyanion $Na_4Fe_3(PO_4)_2(P_2O_7)$ (NFPP), and Li-ion reference cells. Similar to Li-ion, Na-ion performance degrades as temperature decreases; however, all tested Na-ion chemistries retain measurable discharge capacity at −40 °C (51%–62% of the 25 °C value), whereas the Li-ion reference cells did not sustain discharge under the same protocol. Polarisation resistance from electrochemical impedance spectroscopy (EIS) testing across a range of operating temperatures exhibits the Arrhenius-type temperature dependence, with layered oxides showing higher thermal sensitivity ($E_a \approx 70$–$75\,kJ\,mol^{-1}$) than NFPP. Furthermore, temperature-indexed open-circuit voltage (OCV) measurements show that OCV–State of Charge (SOC) relations are both chemistry- and temperature-dependent. Layered oxides exhibit more pronounced low-temperature hysteresis and curve-shape changes, while NFPP remains more consistent within a mid-SOC window. Additionally, voltage-synchronous casing strain is robustly observable for layered oxides (NFM/CFM) under the present mounting configuration; by contrast, no resolved casing-level signature is observed for NFPP. Within NFM, charging at 0 °C exhibits a heavy-tailed constant-voltage duration distribution (outliers > 1000 min), indicating that fixed-voltage termination can induce pack-level SOC imbalance when the cell kinetics are becoming the limiting factor. In strain-enabled ageing measurements, an accumulating residual casing strain follows $\sim \sqrt{t}$ kinetics and correlates with capacity loss in NFM. Long-term cycling shows accelerated capacity fade relative to the other Na-ion chemistries. These results motivate chemistry-specific derating maps, adaptive end-of-charge supervision, pulse-horizon power calibration, and uncertainty-aware, multi-modal SOC and State of Health (SOH) estimation that are required in developing an adequate battery management system for Na-ion batteries.

* Corresponding authors.
*Email addresses:* ml202sl@leeds.ac.uk (S. Liu), k.li1@leeds.ac.uk (K. Li).

https://doi.org/10.1016/j.apenergy.2026.127687
Received 27 March 2025; Received in revised form 28 January 2026; Accepted 9 March 2026
Available online 17 March 2026

**Nomenclature**

*Acronyms*

| | |
|---|---|
| BMS | Battery Management System |
| CC | Constant Current |
| CPE | Constant Phase Element |
| CEI | Cathode Electrolyte Interphase |
| CV | Constant Voltage |
| DCR | Direct Current Resistance |
| DoD | Depth of Discharge |
| DVA | Differential Voltage Analysis |
| ECM | Equivalent Circuit Model |
| EIS | Electrochemical Impedance Spectroscopy |
| ESS | Energy Storage System |
| EV | Electric Vehicle(s) |
| FBG | Fibre Bragg Grating |
| FOI | Feature of Interest |
| GITT | Galvanostatic Intermittent Titration Technique |
| HPPC | Hybrid Pulse Power Characterisation |
| ICA | Incremental Capacity Analysis |
| LIB | Lithium-ion Battery |
| LCO | Lithium cobalt oxide |
| LFP | Lithium iron phosphate |
| Li-ion | Lithium-ion |
| NCA | Lithium nickel cobalt aluminium oxide |
| NMC | Lithium nickel manganese cobalt oxide |
| Na-ion | Sodium-ion |
| NFM | Sodium nickel iron manganese layered oxide |
| CFM | Sodium copper iron manganese layered oxide |
| NFPP | Sodium iron phosphate pyrophosphate |
| OCV | Open-Circuit Voltage |
| PBA | Prussian Blue Analogues |
| RPT | Reference Performance Test |
| SD | Standard Deviation |
| SEI | Solid Electrolyte Interphase |
| SOC | State of Charge |
| SOH | State of Health |
| USABC | United States Advanced Battery Consortium |

*Symbols*

| | |
|---|---|
| $E_a$ | Apparent activation energy (Arrhenius parameter). |
| $I$ | Current. |
| $L_0$ | Inductance. |
| $n$ | Sample size. |
| $P_{\text{pulse}}$ | Pulse power capability. |
| $\text{CPE}_{\text{f}}$ | Film/interphase constant phase element. |
| $\text{CPE}_{\text{dl}}$ | Double-layer constant phase element. |
| $Q$ | Capacity. |
| $R_0$ | Ohmic resistance. |
| $R_{\text{f}}$ | Film/interphase resistance. |
| $R_{\text{ct}}$ | Charge-transfer resistance. |
| $R_{\text{pol}}$ | Polarisation resistance. |
| $R_{\text{pulse}}$ | Pulse resistance. |
| $t$ | Time. |
| $t_0$ | Reference time (initial cycle). |
| $T$ | Temperature. |
| $V$ | Voltage. |
| $V_{\text{max}}$ | Maximum voltage within the defined pulse window. |
| $V_{\text{min}}$ | Minimum voltage within the defined pulse window. |
| $V_{\text{norm}}(t)$ | Normalised terminal voltage within a pulse. |
| $V_{\text{min, pulse}}$ | Minimum discharge pulse voltage. |
| $W_{\text{diff}}$ | Warburg impedance for diffusion. |
| $\text{OCV}_{\text{dis}}$ | Open-circuit voltage during discharge. |

*Greek Symbols*

| | |
|---|---|
| $\Delta\varepsilon_{\text{cum}}(t)$ | Cumulative residual (irreversible) strain relative to the reference point at time $t$. |
| $\varepsilon_{\text{res}}(t)$ | Residual (end-of-cycle) strain at time $t$ under the reference condition. |
| $\varepsilon_{\text{res,0}}$ | Residual strain at $t = t_0$. |

## 1. Introduction

The global expansion of renewable electricity generation and the rapid electrification of transport have intensified demand for energy storage technologies that can be deployed at scale and at low cost [1]. Lithium-ion (Li-ion) batteries remain dominant across many applications, yet their dependence on critical minerals, such as lithium, nickel, graphite, and cobalt, raises concerns about supply chain exposure and price volatility [2]. In this context, sodium-ion (Na-ion) batteries have attracted growing interest because sodium is abundant and comparatively inexpensive. This materials advantage makes Na-ion technology particularly relevant for grid-scale storage and cost-sensitive mobility, where material availability and manufacturability can be as influential as peak gravimetric energy density [3,4].

The commercialisation of Na-ion technology has progressed from prototype demonstration to scaled manufacturing, with early products primarily targeting cost-sensitive stationary storage and short-range mobility [2]. Many contemporary cells adopt standard form factors, such as the cylindrical 18650, which can reduce integration effort within established module and pack manufacturing and assembly practices. However, commercial development is not converging on a single cathode solution, and several cathode families are being pursued in parallel. One route uses layered transition metal oxides (e.g., O3-type materials) and prioritises specific energy, which is typically in the range of 100–160 $\text{Wh kg}^{-1}$ [5,6]. A second route employs polyanionic compounds, while Prussian blue analogues are also increasingly developed, with an emphasis on power capability and kinetic stability, often with lower gravimetric energy [7]. Early deployment indicates that chemistry-dependent signatures can greatly affect the observability and control. Pronounced hard carbon hysteresis and differences in voltage plateau structure are common examples [6,8]. These features limit direct substitution for Li-ion systems and motivate control strategies that are explicitly chemistry-aware.

Early evidence from commercial-cell studies indicates that operability is governed by coupled effects of temperature and State of Charge (SOC) rather than by a single set of fixed limits. As temperature decreases, resistive contributions rise sharply, with both pulse resistance and impedance increasing markedly [7,9]. Beyond temperature effects, Rehm et al. [7] show that SOC also materially influences efficiency and resistance. Losses are substantially larger at low SOC than within higher-SOC windows, especially under constant-power operation, where reduced terminal voltage forces higher current. Crucially, these temperature–SOC sensitivities are accompanied by pronounced cell-to-cell dispersion, which limits the transferability of room-temperature assumptions to cold-start and low-SOC conditions. These operating challenges are compounded at low temperature when fast charging is required, where performance derating gives way to reliability constraints. High charge rates under sub-zero conditions can promote sodium deposition and dendritic growth, elevating the risk of internal short circuits and safety incidents [10]. Such damage may develop before overt failure, manifesting as anode morphological degradation and measurable impedance changes [9,10].

In parallel with these reliability risks, state observability is also less straightforward than in many Li-ion systems. The voltage–SOC

relationship is less deterministic, as low-SOC hysteresis associated with hard carbon, voltage relaxation, and equilibration phenomena (e.g., anode overhang) can bias open-circuit-voltage (OCV)-based calibration and complicate uncertainty-bounded state estimation [6,8,11]. Model development is further complicated by the way supporting measurements are obtained. Half-cell artefacts, particularly when sodium metal counter electrodes introduce large and unstable overpotentials, can distort parameter identification and limit the direct transfer of electrode-level potential data to full-cell calibration [8]. These combined effects suggest that lifetime risk is not captured by gradual capacity fade alone. Reliability assessments highlight failure modes, such as float current divergence and gas-driven activation of current interrupt devices, which motivate monitoring strategies that extend beyond conventional State of Health (SOH) metrics to capture abrupt fault conditions [6,9].

Despite the insights provided by these studies, recent commercial benchmarks using aligned test protocols have primarily reported average energetic and rate-performance metrics, whereas they provide limited evidence on dynamic response characteristics across operating conditions and on cell-to-cell variability required for uncertainty-aware state estimation and operating-limit definition. In addition, mechanical observables may provide an independent monitoring channel for tracking when voltage-based estimates are biased by hysteresis and relaxation. In Li-ion cells, surface strain has proved informative for tracking degradation and identifying incipient failures [12]. For commercial Na-ion cells, however, strain-coupled electrochemical behaviour remains underexplored, and its value for state estimation and fault diagnostics has not been established.

In order to address these gaps, this study implements a harmonised test matrix across temperature and SOC for three commercial sodium-ion chemistries and benchmarks them against mature lithium-ion reference cells. Multiple replicate cells are tested for the primary sodium-ion type to quantify between-cell variability. Specifically, the study establishes temperature-indexed electrical and state-mapping information, including impedance characteristics, SOC–OCV behaviour with hysteresis, and transient response metrics under representative current excitations, enabling uncertainty-aware operating-limit setting by quantifying their dependence on operating conditions and the extent of between-cell variability under aligned comparisons. Finally, in-operando casing strain is evaluated as an auxiliary observable, and long-term cycling is conducted and compared across the three sodium-ion chemistries, thereby identifying which parameter maps and limits are transferable across chemistries and which require chemistry-specific calibration for robust battery management.

The remainder of this paper is organised as follows. Section 2 outlines the materials and methods, including the evaluation protocols and experimental techniques. Section 3 presents the results and associated analysis of the characteristics of the investigated cells. Section 4 discusses the key findings and their implications for chemistry-aware battery management system (BMS) design. Finally, Section 5 concludes the work.

## 2. Materials and methods

### 2.1. Overview of cell properties and evaluation standards

This study investigates a 1.3 Ah, 18650-format cylindrical sodium-ion cell comprising a sodium nickel iron manganese layered oxide ($Na(Ni,Fe,Mn)O_2$, NFM) cathode and a hard carbon anode. The material composition and key specifications are summarised in Table 1. In order to benchmark electrochemical performance against established chemistries, we evaluated reference 18650-format cells employing a sodium copper iron manganese oxide cathode ($Na(Cu,Fe,Mn)O_2$, CFM) and a sodium iron phosphate pyrophosphate cathode ($Na_4Fe_3(PO_4)_2(P_2O_7)$, NFPP), alongside two commercial LIBs, lithium iron phosphate ($LiFePO_4$, LFP) and lithium nickel cobalt aluminium oxide ($Li(Ni,Co,Al)O_2$, NCA). Detailed specifications for these reference cells are provided in Supplementary Tables S1 and S2. In this study, cells are referred to by their cathode chemistries (e.g., NFM, LFP) to facilitate performance comparison, with sodium-ion cell manufacturers undisclosed.

**Table 1**
Material composition and specifications of the investigated NFM cell.

| | |
|---|---|
| **Material composition** | |
| Cathode material* | $Na[Ni_{1/3}Fe_{1/3}Mn_{1/3}]O_2$ |
| Anode material | Hard carbon |
| Electrolyte | Ethyl methyl carbonate with $NaPF_6$ salt |
| Separator | Polyethylene |
| Current collector (cathode & anode) | Aluminium foil |
| Cell housing | Steel mantle |
| **Cell specifications** | |
| Nominal voltage | 3.10 V |
| Nominal capacity | 1300 mAh @ 0.50 C, 25 °C |
| Typical capacity | 1350 mAh @ 0.50 C, 25 °C |
| Charge voltage | 3.95 ± 0.05 V |
| Discharge cut-off voltage | 1.50 ± 0.05 V |
| Internal resistance | ≤ 20.0 mΩ, AC, 25 °C |
| Cell dimensions | Diameter: 18.40 ± 0.10 mm; Height: 65.30 ± 0.10 mm |
| Energy density | 118.00 Wh/kg |
| Weight | 30.00 ± 0.50 g |
| Max. continuous charging rate | 0–45 °C: ≤ 1.00 C; > 45 °C: cannot charge |
| Max. continuous discharge rate | 0–45 °C: ≤ 3.00 C; 45–60 °C: ≤ 0.50 C; > 60 °C: cannot discharge |
| Max. constant charge current (CC) | 1.00 C; CV voltage: 3.95 V; Termination current: 0.05 C |
| Max. constant discharge current | CC: 3.00 C |

* ICP results: Na:Ni:Fe:Mn = 1.0:0.33:0.33:0.34 (atomic); mass fractions: 20, 17, 16, 16 wt%.

To assess the cells' performance, we established a testing protocol that reflects typical usage conditions [13–15]. This approach ensures that the results are directly comparable to those of existing LIBs and provides valuable insights into the cells' potential applications in electric vehicles (EVs) and energy storage systems (ESSs). The evaluation procedures for battery performance and lifetime were adapted from the United States Advanced Battery Consortium (USABC) Battery Test Manual for Electric Vehicles [16]. An overview of the experimental workflow and the corresponding test coverage across chemistries is provided in Fig. 1 and Table 2. The test platforms and instrumentation are shown in Supplementary Fig. S1. Unless stated otherwise, continuously monitored signals were recorded at 1 Hz.

### 2.2. Preconditioning test

To ensure stable cell performance and screen for potential manufacturing defects, preconditioning tests were performed [17]. All cells were placed in a thermal chamber at 25 °C and 50% relative humidity for 4 h prior to testing.

For NFM cells, the preconditioning cycle commenced with charging the cells at a constant current (CC) of 0.5 C, followed by a constant voltage (CV) phase at 3.95 V until the current decreased to 0.05 C. After a 10-minute rest, the cells were discharged at a constant current of 0.5 C down to 1.50 V, followed by another 10-minute rest. This charge–discharge procedure was repeated three times. Reference cells (CFM, NFPP, LFP, and NCA) underwent an identical protocol, with voltage windows and C-rates adapted to their respective chemistries (Supplementary Table S3).

As newly manufactured cells may exhibit capacity fluctuations or rapid performance degradation due to potential production anomalies during initial cycles, cells exhibiting operational anomalies or incomplete current/voltage profiles were excluded. The remaining cells showing a capacity variation within ±2% across the three preconditioning cycles were subsequently selected for further testing.

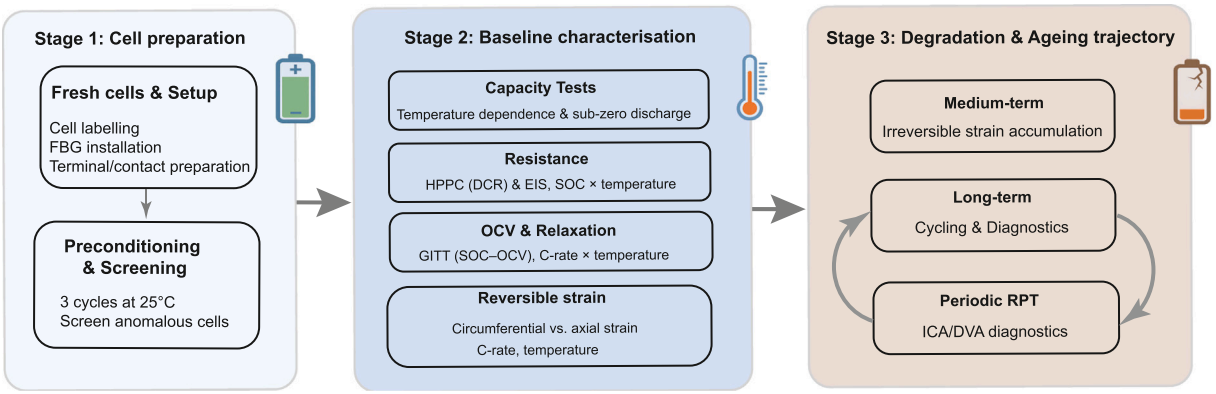


**Fig. 1.** Experimental workflow comprising three stages: (i) preconditioning and screening of fresh cells, (ii) baseline electrochemical and mechanical characterisation (capacity, HPPC/EIS, GITT-based OCV, and FBG strain) across 0–45 °C, and (iii) degradation testing with continuous strain monitoring and periodic RPTs (ICA/DVA).

**Table 2**
Experimental coverage and sample sizes ($n$) across chemistries.

| Chemistry | Precond. (25 °C) | Capacity (0/25/45 °C) | Sub-zero cap. (sub-zero T) | HPPC (pulse and/or DCR) | EIS (0/50/100% SOC) | EIS (5-chem) (50% SOC) | GITT (OCV, Relaxation) | Reversible strain (0/25/45 °C) | Medium-term (Irreversible strain) | Long-term (Cycling + RPT) |
|---|---|---|---|---|---|---|---|---|---|---|
| **NFM** | 25 °C, 3 cyc | 0.5 C | −20/−40 °C 0.2 C | 0/25/45 °C | 0/25/45 °C | −30 to 45 °C | 0/25/45 °C | Axial + Circ. (0.5/0.1 C) | 1 C × 50 cyc | 0.2 C |
| | ($n$ = 40 → 33) | ($n$ = 33) | ($n$ = 3) | ($n$ = 31) | ($n$ = 4) | ($n$ = 2) | 0.1/0.5/1 C ($n$ = 8) | Circ. 0/25/45 °C | ($n$ = 2) | RPT/50 cyc ($n$ = 2) |
| **CFM** | — | — | −20/−40 °C 0.2 C | 25 °C (0.2/0.5/1 C) | — | −30 to 45 °C | 0.5 C only | Circ. 0/25/45 °C | — | 0.5 C |
| | | | ($n$ = 3) | ($n$ = 1) | | ($n$ = 2) | ($n$ = 3) | 0.1 C ($n$ = 1) | | RPT/100 cyc ($n$ = 1) |
| **NFPP** | — | — | −20/−40 °C 0.2 C | 25 °C (0.2/0.5/1 C) | — | −30 to 45 °C | 0.5 C only | Circ. 0/25/45 °C | — | 0.5 C & 1 C |
| | | | ($n$ = 3) | ($n$ = 1) | | ($n$ = 2) | ($n$ = 3) | 0.1 C ($n$ = 1) | | RPT/100 cyc ($n$ = 2) |
| **LFP** | — | — | −20/−40 °C 0.2 C | 25 °C (0.2/0.5/1 C) | — | −15 to 45 °C | — | — | — | — |
| | | | ($n$ = 3) | ($n$ = 1) | | ($n$ = 2) | | | | |
| **NCA** | — | — | −20 °C only 0.2 C | 25 °C (0.2/0.5/1 C) | — | −15 to 45 °C | — | — | — | — |
| | | | ($n$ = 3) | ($n$ = 1) | | ($n$ = 2) | | | | |

### 2.3. Capacity test

In this study, the capacity of NFM cells was evaluated under representative operational temperatures as well as under severe low-temperature conditions. Capacity values were obtained from the CC discharge phase. The test procedure was adapted from IEC 62660–1 for secondary lithium-ion cells used in electric-vehicle applications [18]. The standard specifies representative temperatures of 0 °C, 25 °C, and 45 °C, corresponding to low, average, and high operating conditions, respectively. These temperatures align with the typical operational range for most battery applications (5–45 °C).

For tests conducted at typical operational temperatures, cells were conditioned in a BINDER (LIT MK 240) thermal chamber at the designated temperature for 3 hours before testing to ensure thermal equilibrium. Subsequently, the cells were charged using a CC–CV process with a CC to 3.95 V, followed by CV until the current dropped to 0.05 C. Then, the cells were rested for 60 minutes. Discharge testing was carried out at 0.5 C until the lower cut-off voltage (1.50 V) was reached.

At severe low temperatures (−20 °C and −40 °C), discharge capacity was compared across multiple chemistries. For each chemistry, three cells with fewer than five prior cycles were selected. Cells were first equilibrated at 25 °C for 3 h and charged using a CC–CV protocol at 0.2 C, with a cut-off current of 0.065 A. Subsequently, they were transferred to a thermal chamber at the target sub-zero temperature and held for 3 h prior to discharge at 0.2 C. The test C-rate was selected to mitigate voltage polarisation at low temperatures while maintaining application relevance. The full protocol was repeated three times per cell, with re-equilibration and charging at 25 °C before sub-zero conditioning and discharge at the target sub-zero temperature. NCA cells were not tested at −40 °C as this temperature falls outside the specified operating range.

### 2.4. Internal resistance measurements

The power capability of a battery is governed by its internal resistance, which varies with key parameters, such as temperature, SOC, and SOH [19]. Consequently, characterising this resistance is essential for defining operational boundaries, predicting performance, and monitoring the SOH [19,20]. The Electrochemical Impedance Spectroscopy (EIS) and Hybrid Pulse Power Characterisation (HPPC) tests are the two commonly used methods in LIBs to estimate internal resistance [21]. Studies have shown that LIB's resistances estimated by EIS are lower than those obtained from HPPC tests [21,22]. This difference becomes more pronounced at low temperatures, where the dynamic effects captured by HPPC are more prominent [23]. In this study, we employed both EIS and HPPC to assess the internal resistance of the SIBs.

#### 2.4.1. EIS test

EIS measurements are typically performed by applying a small sinusoidal perturbation and analysing the cell's response [24]. In

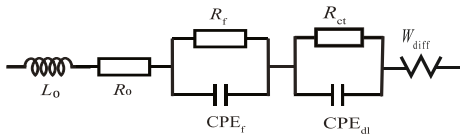


**Fig. 2.** Equivalent circuit model used for EIS fitting comprising: (i) inductance ($L_0$) and ohmic resistance ($R_0$), (ii) an interphase/film-related branch modelled as $R_f \parallel CPE_f$, (iii) a charge-transfer branch modelled as $R_{ct} \parallel CPE_{dl}$, and (iv) a Warburg-type element ($W_{diff}$) representing diffusion-/mass-transport-related impedance at low frequencies.

potentiostatic mode, a sinusoidal potential is applied, and the resulting current is measured. Conversely, in galvanostatic mode, a sinusoidal current is applied, and the corresponding potential response is recorded. Ideally, both methods produce equivalent results, offering flexibility in experimental design [25]. The measured impedance response can be interpreted using a commonly used equivalent circuit model (ECM) shown in Fig. 2. The model includes an inductive contribution ($L_0$), an ohmic contribution ($R_0$), an interphase or film-related branch modelled as $R_f \parallel CPE_f$, and a charge-transfer branch modelled as $R_{ct} \parallel CPE_{dl}$ [21]. At low frequencies, diffusion or mass-transport effects are represented by a Warburg-type element ($W_{diff}$). In the semi-infinite diffusion limit, this contribution gives an approximately 45° tail in the Nyquist plot.

In this study, EIS spectra for the NFM cells were acquired at 0%, 50%, and 100% SOC at three different temperatures (0 °C, 25 °C, and 45 °C) by applying a sinusoidal current. The cells were first discharged to the lower cut-off voltage using 0.1 C rate at 25 °C and then placed in the thermal chamber at 0 °C for more than 3 h. Subsequently, EIS tests were performed on the cells over a frequency range of 0.001 Hz to 10 kHz. During this process, high-frequency EIS measurements were also repeated three times to determine the resistance values. Once the measurements at a given SOC were completed, the thermal chamber was reset to 25 °C with 50% humidity and maintained for 3 h, after which the cells were charged to the next SOC stage using a 0.1 C current. The capacity used for SOC calculations was based on the actual capacity of each cell, as determined from a capacity test conducted at 25 °C. Then, the thermal chamber was set back to the target test temperature and the EIS tests were conducted. The procedures for EIS tests at 50% and 100% SOC were identical to those at 0% SOC. Furthermore, the EIS tests at 25 °C and 45 °C followed the same procedures as those at 0 °C, while the frequency range was set from 0.01 Hz to 10 kHz.

Additional EIS measurements were performed on fresh cells (fewer than 10 cycles) across five chemistries at 50% SOC (set by charging at 0.1 C at 25 °C). Two cells per chemistry were tested at −30 °C, −15 °C, 0 °C, 25 °C, and 45 °C, except that LFP and NCA were not tested at −30 °C because the benchmark measurements were designed around conditions representative of typical operation. The resulting spectra were used to quantify the temperature-dependent polarisation resistance ($R_{pol}$) for subsequent analysis.

#### 2.4.2. HPPC testing

The HPPC method was employed to evaluate cell resistance at specific temperatures and SOC levels. The pulse resistance, $R_{pulse}$, is calculated as the ratio of the voltage change ($\Delta V$) to the current change ($\Delta I$) during a nominal constant-current pulse:

$$R_{pulse} = \frac{\Delta V}{\Delta I} \tag{1}$$

Pulse resistance estimates from HPPC data depend on the sampling time after pulse onset [19,21]. As there is no universally adopted reporting time and practice varies across studies [25], resistance was evaluated at multiple instants in this work. Here, $\Delta V$ was defined as the difference between the terminal voltage immediately before pulse onset and the voltage at $t$ = 1, 5, and 10 s after pulse onset, providing $R_{1s}$, $R_{5s}$, and $R_{10s}$.

This pulse resistance includes ohmic, charge transfer, and polarisation components. Ohmic resistance $(R_0)$ represents the electrical resistances within the cell and is responsible for the instantaneous voltage drop when a current pulse is applied. Charge transfer resistance $(R_{CT})$ is linked to the electrode-electrolyte interfacial reactions and becomes evident a few seconds after pulse initiation. Polarisation resistance $R_{pol}$ is associated with ionic diffusion within the solid phase and often serves as a rate-limiting step in LIBs/SIBs. The contributions of these three components can be calculated individually to provide a clearer understanding of the complex electrochemical processes in the battery system [21,26]. However, when using direct current for resistance measurements, all contributions to resistance are imposed simultaneously, making it challenging to separate the individual components [19]. Therefore, calculating a bulk total cell resistance from the overall voltage drop during the pulse is a common approach in prior studies [27,28].

In order to evaluate the electrochemical resistance of the NFM cells under different operating temperatures, HPPC measurements were conducted at 0 °C, 25 °C, and 45 °C in a thermal chamber with a controlled relative humidity of 50%. An adapted protocol detailed in [21] was employed throughout the experiments. Initially, the cells were fully charged (0.5 C CC–CV charge to 3.95 V, with a current cut-off of 0.05 C) and then allowed to rest for 30 min to stabilise. Subsequently, the cells were discharged at 0.5 C to 90% SOC (referenced against the nominal cell capacity). Each cell was allowed to equilibrate for 60 min before 10 s charge and discharge pulses at 0.2, 0.5, and 1 C were applied, with a 60 s relaxation period between pulses. The cells were then discharged at 0.5 C for an additional 10% SOC decrement to the next breakpoint, and this process was repeated until the cell voltage reached the lower cut-off voltage (1.50 V).

For cross-chemistry comparison of the HPPC discharge-pulse responses, the terminal voltage within each 10 s pulse was normalised as

$$V_{norm}(t) = \frac{V(t) - V_{min}}{V_{max} - V_{min}} \tag{2}$$

where $V_{max}$ and $V_{min}$ denote the maximum and minimum voltages within the defined pulse window, respectively. The pulse window was defined from pulse onset to $t$ = 10 s, with $V_{max}$ taken as the voltage at pulse onset and $V_{min}$ as the voltage at $t$ = 10 s.

From the complete set of test data, individual pulses are extracted based on battery voltage and current. The resistance values under different applied current rates can then be determined for each pulse.

### 2.5. Pulse power capability

Pulse power capability ($P_{pulse}$) was characterised using the HPPC test data at 10% SOC intervals, where the discharge power is defined relative to the minimum discharge pulse voltage ($V_{min,\,pulse}$). These power capability measurements determine the usable depth of discharge (DoD) within specified pulse voltage constraints for a given discharge power level [16]. Previous research has demonstrated that LIBs exhibit marked temperature dependence, with substantial degradation in pulse power performance at reduced temperatures [29]. The pulse power capability during discharge is calculated using Eq. (3):

$$P_{pulse} = \frac{V_{min,\,pulse} \cdot (OCV_{dis} - V_{min,\,pulse})}{R_{pulse,\,discharge}} \tag{3}$$

Battery discharge performance presents distinct challenges compared to charging, particularly under high-power demand scenarios such as electric vehicle acceleration or power-intensive mobile applications [29]. To evaluate the viability of NFM cells for moderate-rate applications, pulse power capabilities were assessed with 1 C discharge

pulses using the HPPC test protocol detailed in Section 2.4.2. These testing conditions were selected to align with the operational requirements of both residential and utility-scale stationary ESSs, as well as EV applications [14,30,31].

### 2.6. Voltage relaxation characterisation and SOC–OCV relationship

Voltage relaxation characterisation is employed to investigate the intrinsic electrochemical processes within batteries by monitoring the evolution of cell voltage over time after the removal of an applied current. This approach yields valuable insights into ion transport dynamics, charge redistribution and degradation phenomena. Extended relaxation periods (typically at least 1 h at room temperature) are required after current removal to allow the cell potential to converge towards its equilibrium value.

By applying a constant current for a fixed duration at different SOC levels, and allowing sufficient relaxation periods after current removal, the SOC–OCV relationship can be established. Studies have shown that the SOC–OCV relationship varies across battery chemistries. For instance, LFP cells exhibit relatively flat OCV–SOC curves and high hysteresis, whereas lithium nickel manganese cobalt oxide (NMC), NCA, and lithium cobalt oxide (LCO) cells display steeper curves and lower hysteresis [32,33]. In addition, working temperature and ageing are key factors that further affect the SOC–OCV relationship [34]. These differences influence the complexity of SOC estimation and the design of BMSs.

The most common method of measuring the OCV versus SOC curves is based on the galvanostatic intermittent titration technique (GITT). This method adjusts the SOC in a stepwise manner and incorporates prolonged relaxation periods to allow the voltage to approach thermodynamic equilibrium [25]. In this work, eight NFM cells were investigated at three C-rates (0.1 C, 0.5 C, and 1 C) at each test temperature (0 °C, 25 °C, and 45 °C). The cells were first discharged to 0% SOC at room temperature. Subsequently, they were placed in a thermal chamber set to the target temperature for 4 h, followed by charging in 10% SOC increments (referenced to the nominal capacity at 25 °C) using a constant-current profile. Between consecutive charge segments, a 2-hour rest period was introduced to allow the cell voltage to re-establish near-equilibrium conditions [35]. To quantify the time required for the voltage to approach this condition, the relaxation time was defined using a drift-rate criterion. For each rest following a GITT pulse, the time to reach $10\,\mathrm{mV\,h^{-1}}$ (i.e., $|dV/dt| < 2.8 \times 10^{-6}\,\mathrm{V\,s^{-1}}$) was determined from the absolute voltage slope estimated by a 10 min rolling-window ordinary least-squares fit. The criterion was required to be met for five consecutive checks at 60 s intervals. If the criterion was not met within the 2-hour rest, the relaxation time was reported as 120 min. The charging process continued in 10% SOC segments until either reaching the upper cut-off voltage (3.95 V) or completing a maximum of 20 segments to provide sufficient coverage of the voltage window at low temperatures. Subsequently, the discharge process followed the same protocol until reaching either the lower cut-off voltage (1.5 V) or 20 segments, maintaining 2-hour relaxation periods between consecutive segments. Throughout this sequence, current, voltage, and the time stamp for each operational step were recorded continuously at 1 Hz. The SOC values were calculated individually for each tested cell using the coulomb counting method. For each cell, SOC was normalised to its total charged capacity with 100% SOC defined at charging completion, and to its total discharged capacity with 0% SOC at discharge completion.

For the reference sodium-ion cells (CFM and NFPP), GITT tests were conducted exclusively at 0.5 C across the three test temperatures (0 °C, 25 °C, and 45 °C). Three cells of each reference chemistry were tested to evaluate cell-to-cell consistency. For each chemistry, the mean SOC–OCV response and the corresponding ± 1 standard deviation (SD) were obtained across the tested cells.

### 2.7. Incremental capacity and differential voltage analysis

Incremental capacity analysis (ICA, dQ/dV) and differential voltage analysis (DVA, dV/dQ) were obtained from the 0.1 C voltage–capacity data. Cells were charged using a 0.1 C CC–CV protocol with a cut-off current of 0.060 A and then discharged at 0.1 C (CC) until the lower voltage cut-off was reached. The analysis procedure was adapted from [36], with minor modifications to reduce numerical-differentiation artefacts. Specifically, data in the vicinity of the upper and lower cut-off regions were excluded prior to differentiation and are therefore not shown in the ICA/DVA plots.

### 2.8. Casing strain measurements

In order to characterise casing-level mechanical response in cylindrical sodium-ion cells, swelling measurements were performed using fibre Bragg grating (FBG) sensors bonded to the external steel casing. Sensors were positioned at approximately mid-height to reduce end-cap boundary effects. After temperature compensation, the measured strain is reported as the external casing strain induced by electrochemically driven dimensional changes during cycling.

Two FBG configurations were implemented on NFM cells to examine directional dependence and rate sensitivity (Supplementary Fig. S2). For circumferential measurements, an FBG sensor was wrapped around the cell and bonded with the fibre oriented along the circumferential direction, providing a measure of hoop strain. For axial measurements, an FBG sensor was aligned parallel to the cylinder axis and positioned within ±0.5 cm of the mid-height to capture axial casing strain. In both configurations, a loosely attached reference FBG sensor placed adjacent to the bonded sensor was used for temperature compensation. Measurements were conducted at 25 °C under constant-current cycling at 0.5 C followed by 0.1 C.

For cross-chemistry and temperature comparisons, the circumferential configuration was used as a consistent measurement geometry. Strain measurements were performed on NFM, CFM, and NFPP cells that had undergone fewer than five prior cycles to reduce ageing-related irreversible strain accumulation. Cells were held at 0 °C, 25 °C, and 45 °C for 4 h prior to testing, then cycled at 0.1 C at each temperature set-point.

The temperature-compensated strain and voltage signals were synchronised, and the differential strain response ($d\varepsilon/dV$) was obtained by numerical differentiation of the strain-voltage curves for charge and discharge using an identical procedure at 0 °C, 25 °C, and 45 °C.

### 2.9. Progression of irreversible strains and capacity fade

To quantify capacity evolution and irreversible strain development under continuous cycling at a 1 C rate, 50 consecutive cycles were executed at 1 C and 25 °C, with the discharge capacity of each cycle recorded as the usable capacity. The nominal capacity after the experiment was determined using a 0.5 C rate.

Simultaneously, casing-level strain was continuously monitored during cycling using circumferentially mounted FBG sensors identical to those described in Section 2.8. This configuration was employed to track the accumulation of non-recoverable strain over successive cycles.

In this work, cumulative residual strain is used as a quantitative metric to characterise the progressive accumulation of end-of-cycle residual deformation during cycling. The cumulative residual strain is defined as the absolute increment of the residual (end-of-cycle) strain

$$\Delta\varepsilon_{\mathrm{cum}}(t) = \varepsilon_{\mathrm{res}}(t) - \varepsilon_{\mathrm{res},0}, \tag{4}$$

where $\varepsilon_{\mathrm{res}}(t)$ denotes the residual strain measured at the end of each cycle under the same reference condition, $\varepsilon_{\mathrm{res},0}$ is the residual strain at the chosen reference point, and $\Delta\varepsilon_{\mathrm{cum}}(t)$ is expressed in $\mu\varepsilon$.

### 2.10. Long-term cycling protocol and ageing diagnostics

Long-term cycling tests were conducted to evaluate the ageing behaviour of the investigated sodium-ion cells under fixed voltage windows, using CC–CV charging and CC discharging profiles. Two NFM cells from different production batches, one CFM cell, and two NFPP cells were selected for this assessment. For the NFM chemistry, preliminary tests at the standard cycling rate indicated that some cells failed before the end-of-life criterion was reached (e.g., 80% SOH), leading to premature test termination. A reduced cycling rate of 0.2 C was therefore adopted for the NFM cells to ensure that complete long-term ageing trajectories could be obtained. The CFM cell was cycled at the standard rate of 0.5 C. For NFPP, one cell was cycled at 0.5 C (standard rate), while the second was cycled at 1 C to examine performance at a higher C-rate.

SOH was defined as the discharge capacity normalised to the maximum discharge capacity recorded for each cell over the entire cycling under identical test conditions, enabling direct comparison of capacity-fade trajectories across the tested chemistries and C-rates.

To provide a consistent diagnostic baseline, periodic reference performance tests (RPTs) were conducted at 0.1 C and 25 °C. RPTs were performed every 50 cycles for the NFM cells and every 100 cycles for the CFM and NFPP cells. The voltage-capacity curves obtained from these RPTs were used for incremental capacity analysis (ICA, dQ/dV) and differential voltage analysis (DVA, dV/dQ) to track the evolution of diagnostic features during ageing.

## 3. Results and discussion

Preconditioning tests were conducted on 40 NFM cells acquired from two procurement orders. Due to uncertainty about the uniformity of production conditions, the cells were labelled as NFM1 and NFM2 to distinguish the batches. Cells exhibiting operational anomalies during preconditioning or subsequent tests (such as voltage shutdown during cycling or complete failure at 0 °C) were excluded. Consequently, 33 cells remained for detailed analysis. Similar voltage-shutdown behaviour has been reported in [6]. They identified that internal pressure buildup, caused by gassing side reactions, can trigger the cell's internal protective devices (CID) to disconnect the circuit.

The same preconditioning and screening procedure was also applied to the reference chemistries prior to their use in benchmark comparisons across chemistries.

### 3.1. Capacity test results and analysis

#### 3.1.1. Analysis of temperature-dependent capacity variation

Fig. 3 shows capacity measurements across 33 NFM cells, identified by their batch designation (NFM1, NFM2) and unique numerical identifiers (e.g., NFM1-1, NFM2-10). The cells exhibited stable discharge capacity at moderate (25 °C) and elevated (45 °C) temperatures, yet displayed considerable performance divergence at 0 °C. Statistical analysis (Fig. 3b) revealed tightly clustered capacity distributions at both 25 °C and 45 °C. The highest discharge capacities were observed at 45 °C, with mean and maximum values of 1.33 Ah and 1.40 Ah, respectively, reflecting the favourable electrochemical kinetics at elevated temperatures. In contrast, low-temperature operation (0 °C) yielded a diminished mean capacity of 1.17 Ah, with a markedly broader distribution range (1.10–1.25 Ah), underscoring substantial cell-to-cell variations.

Analysis of temperature-normalised capacity ratios (Fig. 3c) provides deeper insights into thermal performance dependencies. At 45 °C, the cells maintained consistently elevated capacity ratios of approximately 1.05 relative to their performance at room temperature, with one cell even reaching 1.10. This uniform enhancement suggests robust high-temperature stability across the cell population. The low-temperature regime (0 °C) revealed marked performance heterogeneity, with capacity ratios spanning 0.90–0.95. Such variation is consistent with reduced transport and reaction rates at low temperature.

A comparison between the NFM1 and NFM2 batches reveals modest and temperature-dependent batch differences in discharge capacity (Fig. 4; Table 3). The two batches exhibit comparable mean capacities at 0 °C and 45 °C, with no statistically significant differences observed. In contrast, at 25 °C, NFM2 displays a slightly higher mean discharge capacity than NFM1 (approximately 1.5%), and this difference is statistically significant (Welch's two-sample $t$-test, $p < 0.01$; see Supplementary Methods, S1).

Under severe sub-zero conditions, all chemistries delivered lower discharge capacity at −20 °C than at 25 °C. At −40 °C, the lithium-ion reference cells did not sustain discharge sufficiently to yield a measurable capacity under the present protocol and are therefore not reported. In contrast, all three sodium-ion chemistries retained measurable capacity, with −40 °C retentions of 51–62% relative to 25 °C. Consistently, the Na-ion cells also showed higher capacity retention at −20 °C than the lithium-ion cells (87-90% versus 72%–75%). Among the sodium-ion chemistries, CFM exhibited the highest low-temperature capacity retention at both −20 °C and −40 °C (Fig. 5b).

#### 3.1.2. Distributions of charging and discharging durations

Capacity testing revealed substantial cell-to-cell dispersion in both charging and discharging durations under identical termination criteria. This dispersion is operationally important because it can induce SOC imbalance and non-uniform heat generation at pack level, particularly under cold-start charging.

Fig. 6 presents temporal distribution analyses at 0 °C, 25 °C, and 45 °C, with data binned into 10 intervals (N = 33 cells). At 0 °C, charging durations exhibit broad distribution centred approximately at 500 min, with several cells requiring over 1,000 min (Fig. 6(a). In contrast, cells at 25 °C and 45 °C demonstrate markedly condensed distributions around 120 min (Figs. 6b,c). The 25 °C distribution reveals subtle positive skewness, whilst the 45 °C data shows pronounced right-skewed characteristics, indicating isolated instances of extended charging periods.

Detailed analysis of CC–CV sub-phases (Figs. 6d–i) reveals distinct temperature-dependent behaviours. The CC phase at 0 °C spans 150–300 min with quasi-symmetric distribution. Room temperature and elevated temperature operations demonstrate accelerated CC phases, with mean durations reduced by approximately 43%. This acceleration stems from enhanced ionic mobility and subsequent electrochemical kinetics at higher temperatures [37].

The CV phase emerges as the primary contributor to the large charging duration variability. At 0 °C, it can vary from as little as 100 min to more than 1,000 min (Fig. 6g). While many cells complete CV quickly, a substantial right tail indicates that some cells require prolonged durations, presumably due to slower reaction rates and reduced ionic conductivity [38]. At 25 °C and 45 °C, the CV phase shows narrower distributions with a single dominant peak (Figs. 6h,i). However, at 45 °C, frequent outliers and increased skewness suggest that elevated temperatures can introduce new forms of cell-to-cell variability, possibly from localised overheating or non-uniform reaction kinetics [37].

Discharge characteristics (Figs. 6j–l) maintain relative symmetry across all temperatures, with subtle duration extensions at elevated temperatures. This is consistent with reduced polarisation and lower effective resistance at elevated temperature, which can delay reaching the cut-off voltage within a fixed voltage window and yield slightly higher usable capacity [39,40]. Notably, ambient and elevated temperature discharge profiles demonstrate enhanced uniformity, suggesting improved kinetic homogeneity above 0 °C.

***Remarks:*** Capacity and time-domain characterisation of the 33 screened NFM cells shows clear temperature dependence, and severe sub-zero benchmark tests across chemistries indicate the following.

(i) At 45 °C, discharge capacity is highest (mean 1.33 Ah; max 1.40 Ah), whereas at 0 °C the mean capacity decreases to 1.17 Ah

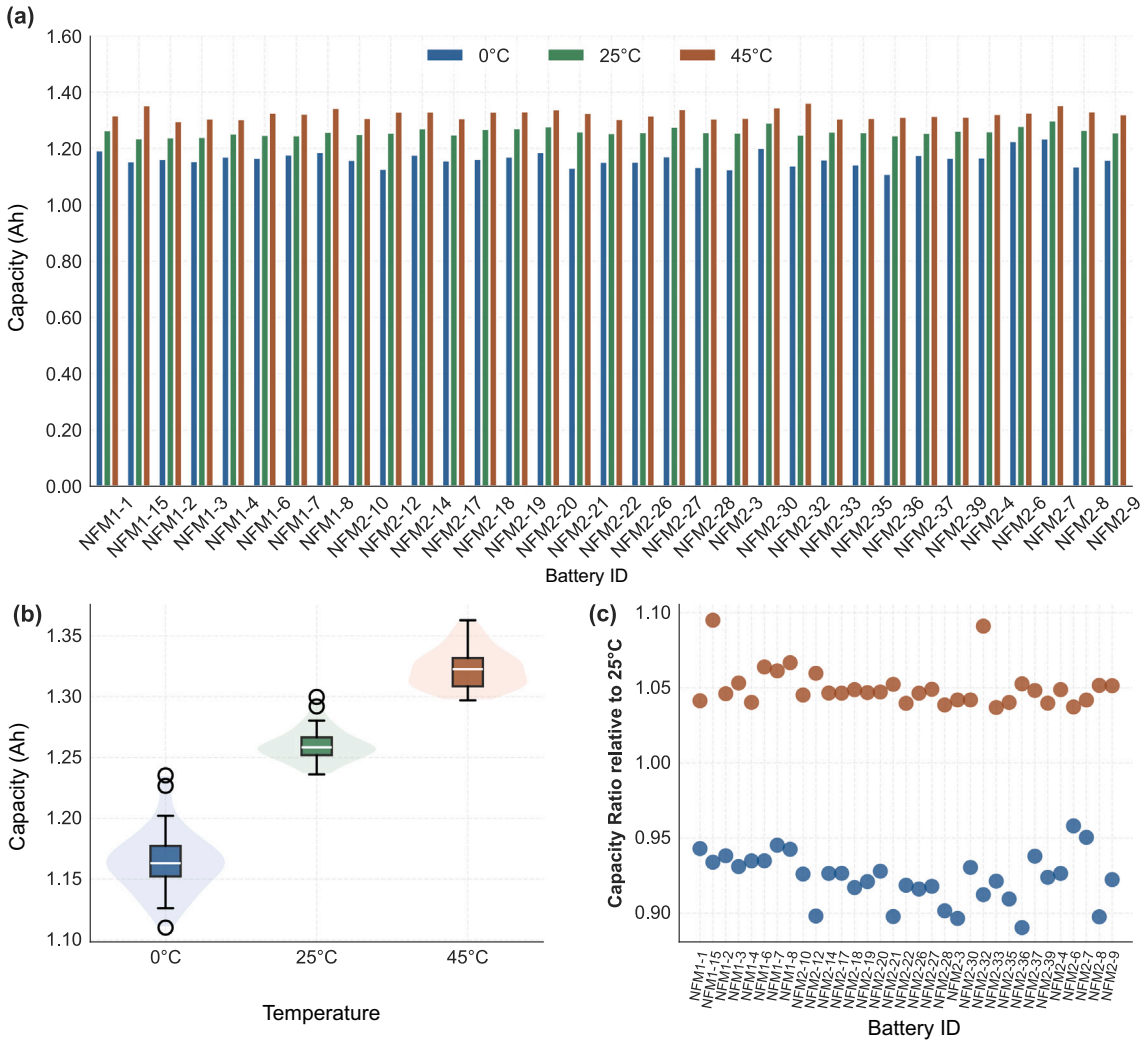


**Fig. 3.** Electrochemical capacity analysis of NFM cells: (a) measured discharge capacities of individual cells at 0 °C, 25 °C, and 45 °C; (b) statistical capacity distributions across the temperature range; (c) temperature-dependent capacity ratios normalised to room temperature (25 °C) performance.

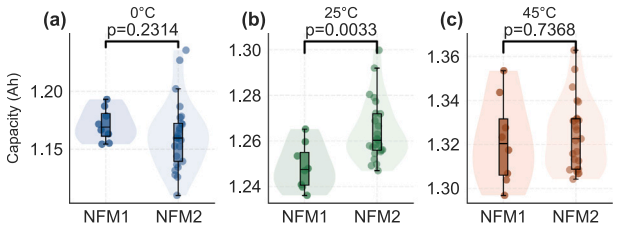


**Fig. 4.** Statistical comparison of discharge capacities between NFM1 and NFM2 battery batches at various temperatures.

**Table 3**
Statistical comparison of discharge capacities between NFM1 and NFM2 battery batches at various temperatures.

| T | NFM1 Mean ± SD (Ah) | NFM2 Mean ± SD (Ah) | *p*-value |
|---|---|---|---|
| 0 °C | 1.171 ± 0.014 | 1.162 ± 0.030 | $0.2314^{ns}$ |
| 25 °C | 1.249 ± 0.010 | 1.264 ± 0.013 | $0.0033^{**}$ |
| 45 °C | 1.322 ± 0.020 | 1.324 ± 0.016 | $0.7368^{ns}$ |

$^{ns}$not significant ($p \geq 0.05$), $^{*}p < 0.05$, $^{**}p < 0.01$, $^{***}p < 0.001$.

with a broader spread (1.10–1.25 Ah; normalised ratio 0.90–0.95 relative to 25 °C).

(ii) Under the present severe sub-zero benchmark protocol, Na-ion chemistries retain measurable capacity at −40 °C (51%–62% of 25 °C), whereas the Li-ion reference cells do not sustain discharge to the cut-off voltage; at −20 °C, Na-ion retention (87%–90%) exceeds Li-ion (72%–75%).

(iii) Time-domain metrics highlight greater dispersion under cold conditions, with total charging duration at 0 °C broadly distributed (centred near ~500 min, with outliers exceeding 1,000 min), whereas at 25 °C and 45 °C it clusters near ~120 min, with the CV phase dominating the spread at 0 °C.

These quantified dispersions provide direct inputs for temperature-aware charging supervision, pack balancing strategy, and uncertainty-aware SOC management.

### 3.2. Resistance analysis from EIS and HPPC characterisation

This section reports resistance and polarisation characterisation using EIS and HPPC across temperature and SOC. EIS is used to quantify the evolution of impedance features and the Arrhenius trends in $R_{pol}$,

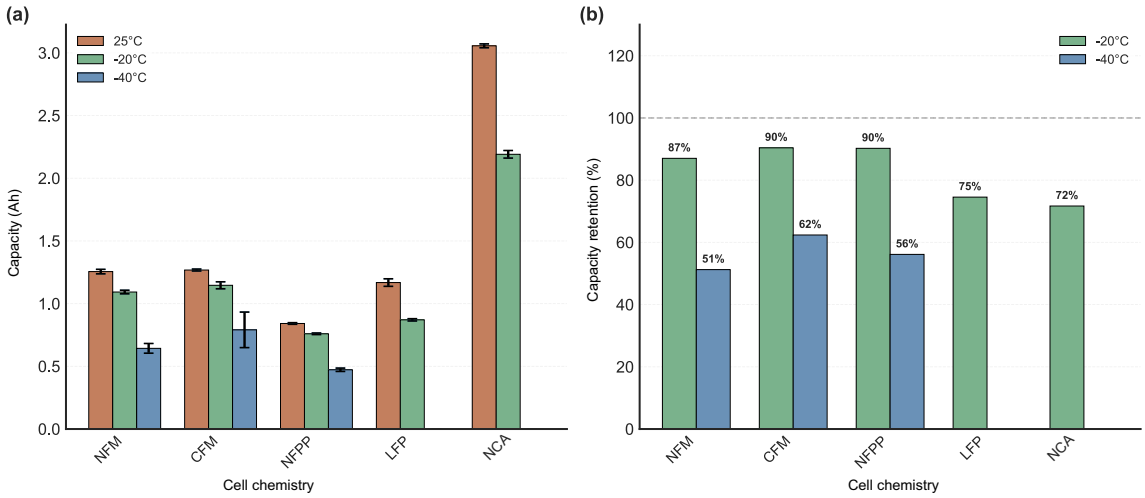


**Fig. 5.** Discharge performance of Li-ion and Na-ion 18650 cells. (a) Discharge capacity at 0.2 C measured at 25 °C, −20 °C and −40 °C for five cell chemistries, defined by their cathode type (NFM, CFM, NFPP, LFP and NCA). Error bars represent ±1 s.d. ($n = 3$). (b) Capacity retention at −20 °C and −40 °C, normalised to the corresponding 25 °C value for each chemistry.

including a cross-chemistry comparison across the five cell types, while HPPC provides pulse-response analysis and time-scale-dependent DCR metrics.

### 3.2.1. EIS measurement results and analysis

Nyquist spectra from four representative NFM cells (NFM2-10, NFM2-19, NFM2-27 and NFM2-28) measured at 0 °C, 25 °C and 45 °C and at three SOC levels (0%, 50% and 100%) are shown in Fig. 7. Across the four cells, the spectra share a consistent overall morphology, comprising a mid-frequency arc followed by a low-frequency tail, with the overall magnitude strongly dependent on operating temperature and SOC. As temperature decreases, the impedance expands markedly, with the largest response occurring at 0 °C. The SOC dependence is most pronounced at 0 °C, where the 0% SOC spectra dominate the mid-to-low-frequency region for all four cells, whereas the 50% and 100% SOC spectra remain comparatively compact. Insets highlight the high-frequency region near the real-axis intercept, where differences across SOC and cells are relatively small compared with the pronounced changes in the main arc at low temperature.

The most pronounced SOC effect is observed at 0% SOC, where the mid-frequency arc enlarges substantially, particularly at 0 °C, indicating strongly increased polarisation under cold and low-SOC operation. This trend is consistent with the extended charging durations reported in Fig. 6 and suggests that charge acceptance and power capability are most constrained near end-of-discharge in sub-zero conditions. At low SOC, no distinct high-frequency feature can be consistently resolved as a separate interphase-related contribution within the measured frequency window, in contrast to the additional high-frequency semicircle often reported for some Li-ion cells [41,42].

Moreover, in the low-frequency region of Fig. 7, a diffusion-like terminal tail is clearly expressed at 45 °C, whereas at 0 °C over the same frequency window the tail is less pronounced and the response remains dominated by the preceding polarisation feature. Notably, the 45 °C tail does not follow the canonical 45° line expected for semi-infinite Warburg diffusion; instead, it exhibits an evident curvature and a slope that departs from 45°, indicating non-ideal diffusion behaviour within the measured frequency range.

Fig. 8 compares the early-life impedance response of five chemistries at −30 °C, −15 °C, 0 °C, 25 °C, and 45 °C. In the low-frequency region, the impedance trajectories deviate from the ideal 45° diffusion tail expected for semi-infinite Warburg behaviour, most notably for NFM and CFM. To capture this non-ideal low-frequency tail consistently across chemistries, the diffusion-related response was represented using a constant phase element within a fractional-order ECM (Supplementary Methods, S2).

Across all chemistries, impedance increases with decreasing temperature, accompanied by an enlargement of the mid-frequency polarisation feature. At 25 °C, replicate cells within each chemistry show good consistency, indicating limited cell-to-cell dispersion under mild conditions. At 45 °C, impedance is lower overall, although consistency between replicates is reduced relative to 25 °C. At sub-zero temperatures, dispersion becomes apparent, particularly in the low-frequency region. Across the set, NFM exhibits the largest mid-frequency arc at low temperatures, and CFM shows similarly elevated polarisation compared with NFPP, LFP and NCA.

The temperature dependence of polarisation is summarised in Fig. 9. Shaded bands indicate the $\pm 1\sigma$ scatter in $\ln(R_{pol})$ around the fitted Arrhenius trends (see Supplementary Methods, S3). The polarisation resistance was taken as the sum of the fitted film-related resistance and the charge-transfer resistance from the ECM, because the film contribution was not consistently resolved as a distinct feature from the charge-transfer response under all conditions. Across all chemistries, $\ln(R_{pol})$ varies approximately linearly with $1000/T$, indicating that the temperature dependence of polarisation is well described by an Arrhenius relationship. The apparent activation energies are 71.6 kJ mol$^{-1}$ (NFM, $R^2 = 0.995$), 74.8 kJ mol$^{-1}$ (CFM, $R^2 = 0.982$), 58.9 kJ mol$^{-1}$ (NFPP, $R^2 = 0.881$), 68.8 kJ mol$^{-1}$ (LFP, $R^2 = 0.919$) and 51.6 kJ mol$^{-1}$ (NCA, $R^2 = 0.955$). This contrast indicates that CFM is more temperature-sensitive, showing a steeper increase in polarisation as temperature decreases, whereas NFM remains more strongly polarised even under moderate conditions. From an operational perspective, this suggests that CFM will exhibit a more rapid deterioration in power capability as ambient temperature falls, while NFM is expected to incur larger overpotentials and greater efficiency penalties across the full temperature range considered. NFPP shows an intermediate response, with a more moderate temperature dependence and correspondingly moderate low-temperature limitations relative to CFM and NFM.

### 3.2.2. HPPC test results and analysis

In the HPPC tests, NFM cells demonstrated distinct temperature-dependent behaviour patterns. While exhibiting relatively stable performance at both 25 °C and 45 °C, the cells encountered significant limitations at 0 °C. In addition, several NFM cells reached the upper voltage limit during the charge pulses at the 90% SOC breakpoint,

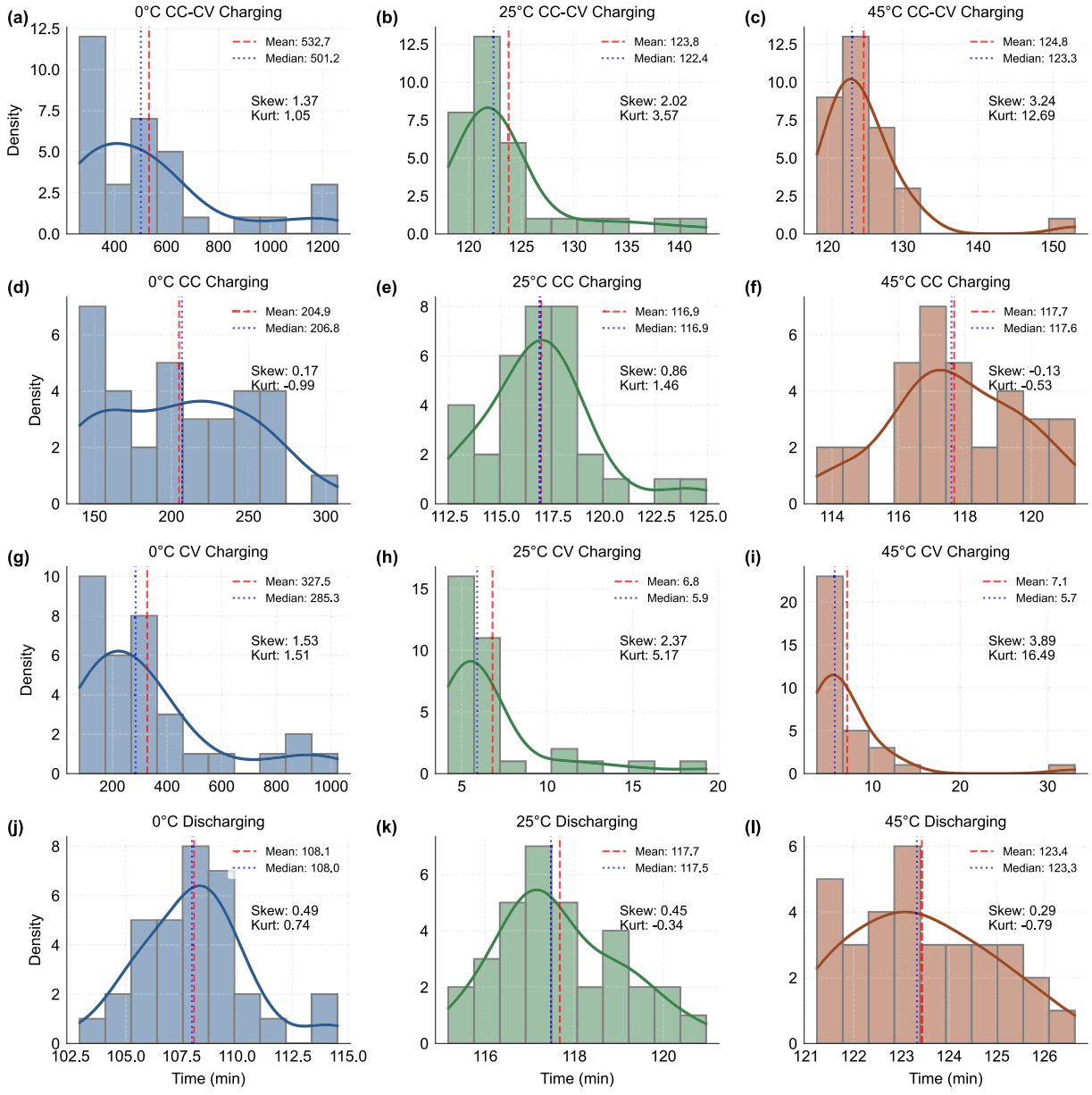


**Fig. 6.** Statistical distributions of charging and discharging durations across multiple temperature conditions (0 °C, 25 °C, and 45 °C). (a-c) CC-CV charging phase distributions; (d-f) CC charging phase distributions; (g-i) CV charging phase distributions; (j-l) discharging phase distributions. Each subplot shows the distribution density with mean (red dashed line) and median (blue dotted line) values, along with skewness and kurtosis metrics.

leading to premature termination of the HPPC sequence. From the initial test group, 31 NFM cells successfully completed the comprehensive measurements across all temperature conditions, as illustrated in Fig. 10. At low SOC and reduced temperature, the voltage response became more heterogeneous across cells, suggesting that sodium-ion chemistry responds more strongly to these operating conditions.

Voltage response analysis at 25 °C reveals chemistry-dependent pulse response behaviour. Fig. 11 compares the normalised voltage response during 10 s HPPC discharge pulses at 0.2 C, 0.5 C, and 1 C (0.1 s sampling). The voltage profiles are normalised within the selected analysis window to enable cross-chemistry comparison of response shape. At approximately 50% SOC, NFM exhibits the largest total voltage drop across the tested C-rates (167 mV at 1 C) and the largest within-pulse time-dependent component at 1 C (144 mV), indicating pronounced polarisation build-up over the 10 s pulse. CFM and NFPP show smaller drops and more limited within-pulse components in absolute magnitude at 1 C (55 mV and 39 mV, respectively). In contrast, NCA shows a step-dominated response, with 81% of the total voltage drop captured at the first post-onset sample (0.1 s after pulse onset) and only a limited additional within-pulse component over the remainder of the pulse (25 mV). LFP exhibits a drift-dominated response with negligible early-time drop, giving a 1 C total drop of 73 mV that is almost entirely within-pulse decay. This chemistry-dependent partitioning between the 0.1 s component and the subsequent within-pulse component is also observed at 20%, and 80% SOC, with the early-time fraction becoming more pronounced for CFM and LFP at high SOC (Supplementary Fig. S3). At 0.2 C and 0.5 C, the early-time component as captured by the 0.1 s sample is negligible for most chemistries at 50% SOC, and the voltage evolution is dominated by slower polarisation processes. After pulse termination, all cells recover rapidly, with NFM showing

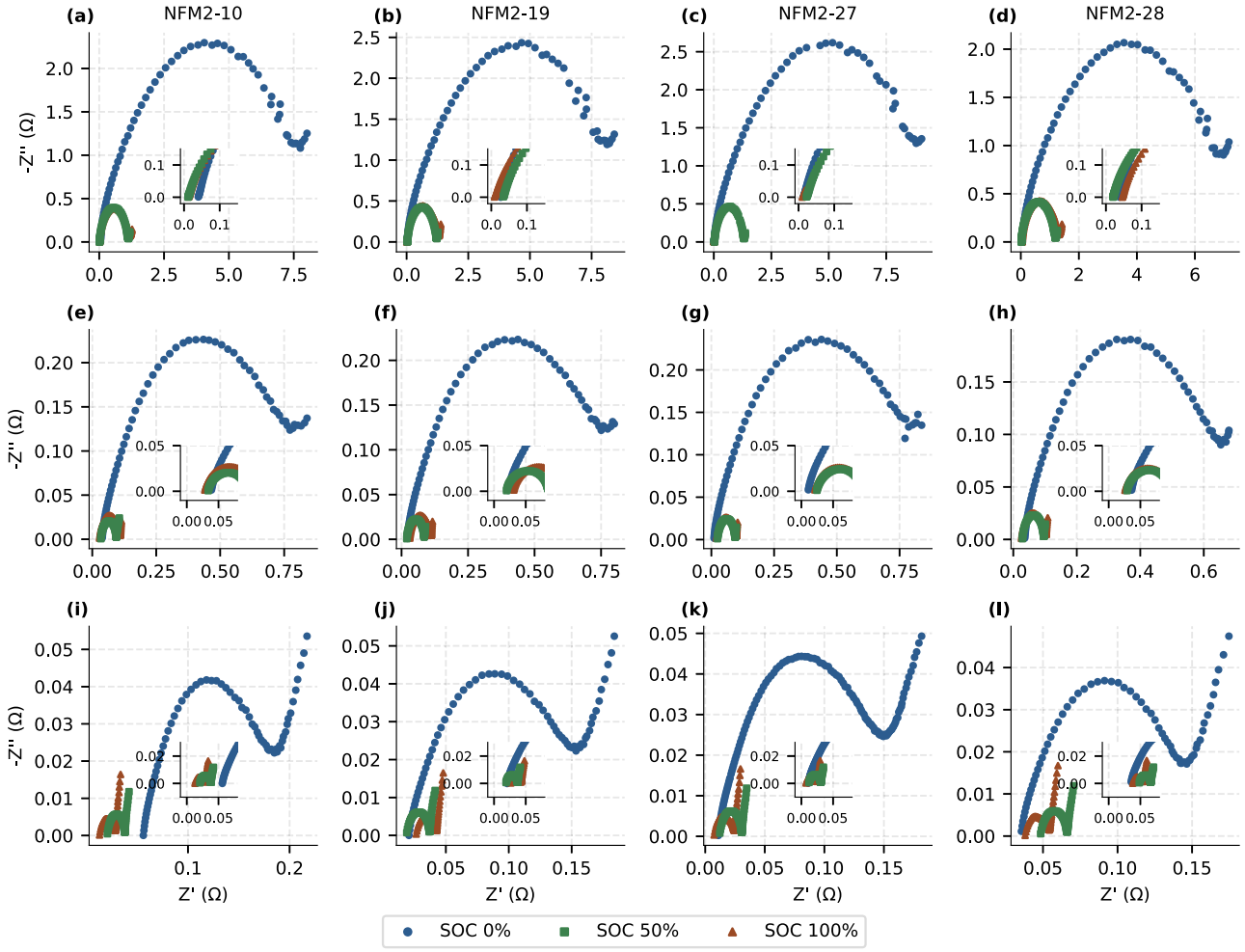


**Fig. 7.** Raw Electrochemical impedance spectroscopy (EIS) spectra of four representative cells measured at 0 °C, 25 °C, and 45 °C (from top to bottom) and at 0%, 50% and 100% SOC. Insets magnify the high-frequency region near the real-axis intercept.

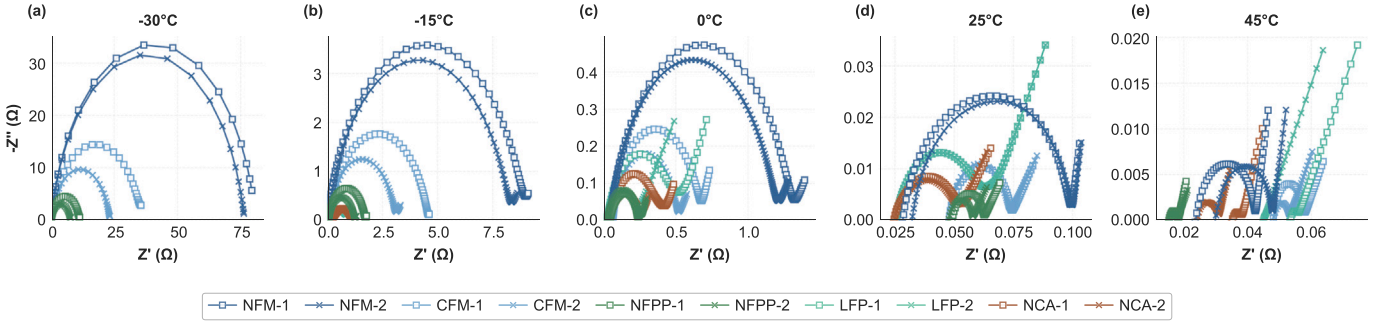


**Fig. 8.** Electrochemical impedance spectroscopy (EIS) comparison of five cell chemistries measured at −30 °C, −15 °C, 0 °C, 25 °C, and 45 °C. (a–e) Nyquist plots at the corresponding temperatures. Two cells are tested for each chemistry. These spectra were used for fractional-order ECM fitting.

the largest recovery ratio (0.92 of the pulse-induced drop recovered within 1 s, compared with 0.63–0.89 for the other chemistries, with LFP the lowest). Key pulse metrics are summarised in Supplementary Table S4, and the 1 C partitioning is reported in Supplementary Table S5. These signatures reflect the balance between an early-time step-like component and a slower polarisation component. Differences in $Na^+$ transport and interfacial processes, including its larger ionic radius and distinct solvation/desolvation behaviour, may contribute to the more pronounced time-dependent response observed for the sodium-ion cells [43].

### 3.2.3. HPPC-derived direct current resistance (DCR) estimation and SOC dependence

Following the definition in Section 2.4.2, pulse resistance was evaluated at multiple instants after pulse onset, yielding $R_{1s}$, $R_{5s}$, and $R_{10s}$ based on $\Delta V$ measured at $t = 1$ s, 5 s, and 10 s. Fig. 12 compares DCR estimates at these sampling instants with EIS-derived resistance at around 50% SOC for four representative NFM cells. This comparison illustrates the sampling-time sensitivity of HPPC-derived resistance, which is most evident at 0 °C, while the DCR estimates at 25 °C and 45 °C are more closely grouped. Motivated by this sensitivity check, the

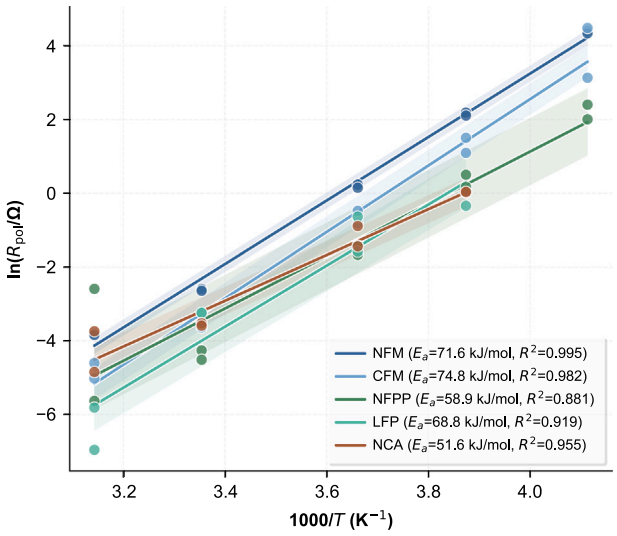


**Fig. 9.** Arrhenius analysis of the temperature dependence of polarisation based on EIS measurements at −30 °C, −15 °C, 0 °C, 25 °C, and 45 °C.

SOC-resolved statistics in Fig. 13 use $R_{10s}$ at 0 °C (1 C pulses), whereas at 25 °C and 45 °C the DCR values represent the average of those calculated from 0.2 C, 0.5 C, and 1 C pulses (using $R_{1s}$). At each sampling instant, the SOC was determined from the ratio of the integrated discharged capacity (from the beginning of discharge to that moment) to the total discharged capacity accumulated over the entire HPPC process. The vertical axis markers in each violin plot denote the average SOC in each data group.

It is evident that at 25 °C and 45 °C, the mean resistance increases as SOC decreases, showing a pronounced rise once SOC falls below 20% and peaking near 0%. Furthermore, the resistance at 25 °C is approximately twice that observed at 45 °C. Under 0 °C, the resistance at each SOC stage exhibits greater variability. For instance, at 90% and 80% SOC, the estimated resistance values range from 0.1Ω to 0.5Ω. From approximately 70% SOC onward, the data become relatively concentrated around the mean, and the overall trend indicates an increase in resistance with decreasing SOC. However, at lower SOC, the variance becomes large once again. These trends indicate that temperature-specific SOC operating windows and power limits should be defined using resistance-based constraints, particularly under sub-zero conditions. Supporting analyses for the two NFM batches across temperature are provided in Supplementary Tables S6–S8 and Supplementary Fig. S4.

***Remarks:*** Resistance characterisation using HPPC-derived DCR, together with EIS, reveals strong time-scale, temperature and chemistry effects relevant to power-limiting and model parameterisation.

(i) Impedance increases markedly with decreasing temperature and shows chemistry-dependent low-frequency non-ideality. Arrhenius trends in $\ln(R_{pol})$ versus $1000/T$ yield activation energies of 71.6 kJ mol$^{-1}$ (NFM), 74.8 kJ mol$^{-1}$ (CFM), 58.9 kJ mol$^{-1}$ (NFPP), 68.8 kJ mol$^{-1}$ (LFP) and 51.6 kJ mol$^{-1}$ (NCA) over −30 °C to 45 °C.

(ii) At 25 °C (around 50% SOC, 1 C), pulse responses show chemistry-dependent partitioning between early-time and within-pulse contributions: NFM exhibits the largest total drop (167 mV) and within-pulse decay (144 mV), whereas CFM and NFPP show smaller total drops (55 mV and 39 mV). NCA is step-dominated (81% captured at 0.1 s), while LFP is drift-dominated, with a 1 C total drop of 73 mV that is almost entirely within-pulse decay.

(iii) Pulse-derived DCR exceeds EIS across the tested conditions and rises steeply at low SOC. At around 50% SOC, DCR can be up to ~10× higher than the EIS-derived resistance at 0 °C, and several-fold higher at 25 °C and 45 °C (Fig. 12). At 25 °C and 45 °C, different $\Delta V$ sampling instants yield similar DCR estimates. Across the cell set, mean resistance increases sharply below ~20% SOC at 25 °C and 45 °C, whereas at 0 °C dispersion is large (e.g., 0.1–0.5 Ω at 80–90% SOC).

These results support pulse-based, temperature- and SOC-dependent resistance constraints for power limits and motivate chemistry-aware parameter updating in control-oriented models.

### 3.3. Analysis of pulse power capability

The $R_{pulse,\ discharge}$ was determined using the $R_{1s}$ values calculated in Section 3.2.3, while the OCV was established from the voltage measured

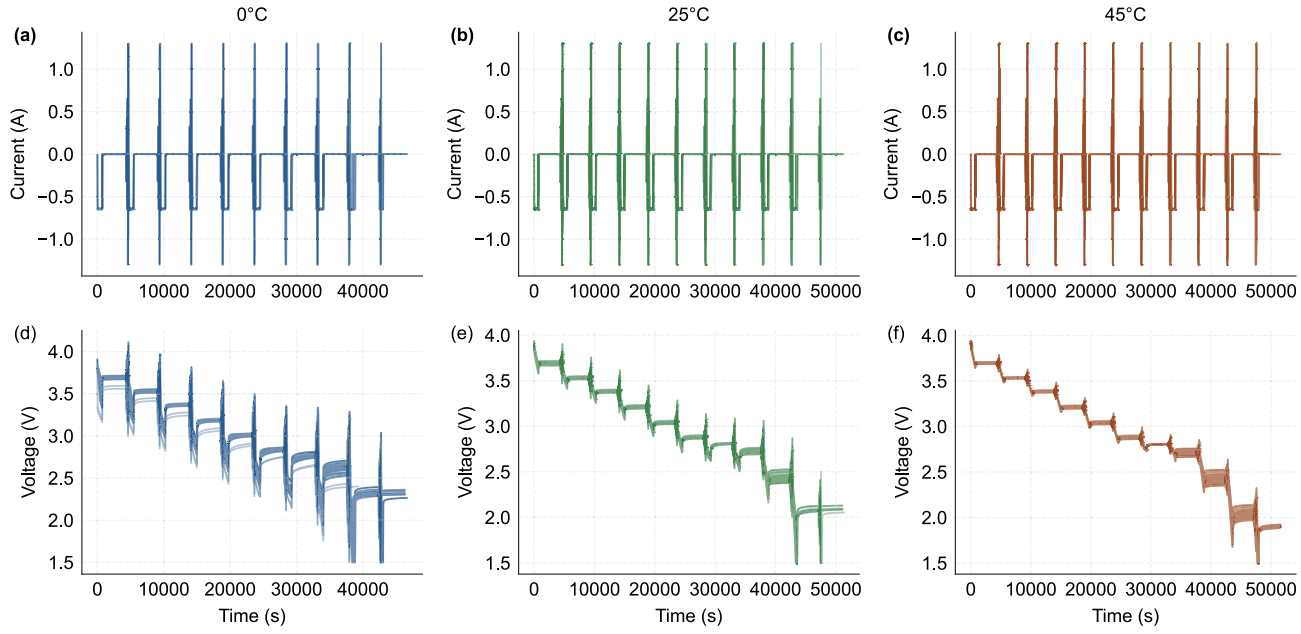


**Fig. 10.** Hybrid Pulse Power Characterisation (HPPC) profiles across 27 sodium-ion cells at 0 °C, 25 °C, and 45 °C, with varying colour intensities denoting individual cell responses.

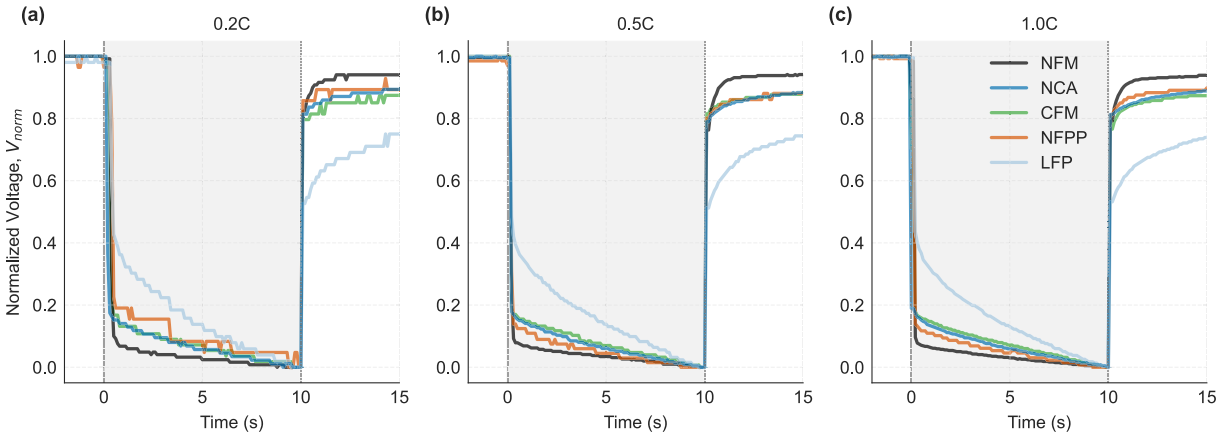


**Fig. 11.** Comparison of normalized voltage responses during HPPC discharge pulses for Na-ion (NFM, CFM, NFPP) and Li-ion (LFP, NCA) cells at 50% SOC. (a) 0.2 C rate, (b) 0.5 C rate, and (c) 1.0 C rate.

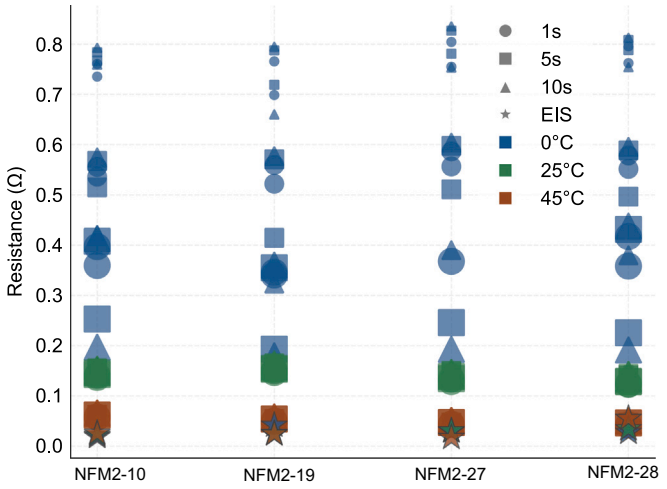


**Fig. 12.** Comparison of HPPC-derived DCR ($R_{1s}$, $R_{5s}$, $R_{10s}$) and EIS-derived resistance at ~50% SOC for four NFM cells. Marker size indicates pulse C-rate and colours denote temperature.

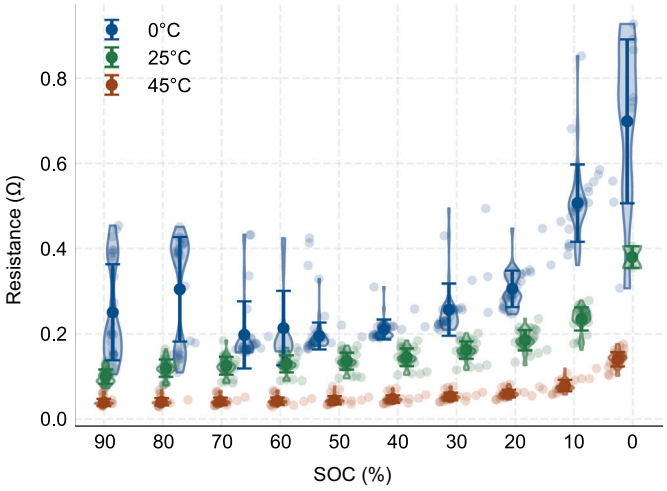


**Fig. 13.** SOC dependence of HPPC-derived DCR under 0 °C, 25 °C and 45 °C. Violin width indicates data density; markers show individual estimates and error bars show mean ± standard deviation (whiskers: non-outlier range).

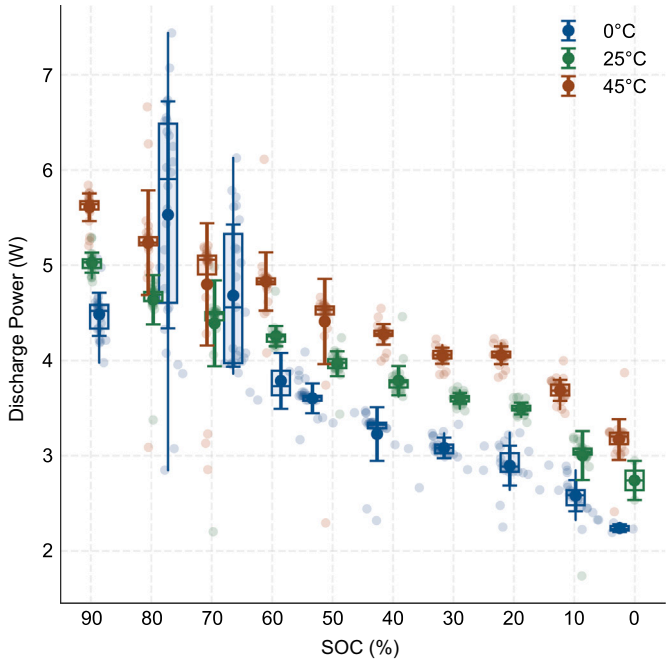


**Fig. 14.** Changes in discharge pulse power capability with SOC at different temperatures. Points represent individual cells (near integer SOC). Boxplots show median and interquartile range with non-outlier whiskers; the larger marker indicates the mean and error bars show ±1 SD.

near the termination of the 60-minute relaxation period. Fig. 14 presents the statistical analysis of temperature and SOC-dependent pulse power capabilities obtained from 27 tested cells.

The pulse power capability exhibits pronounced temperature dependence, with the NFM cells demonstrating maximum mean values at 45 °C. The pulse power capability spans approximately 7 W to 2 W across an SOC range of 90% to 0%. Measurements conducted at 25 °C yielded lower values compared to those at 45 °C, while maintaining similar distribution patterns. The average pulse power capability at 0 °C demonstrates notably reduced performance compared to 25 °C, particularly within the SOC range of 60% to 0%. Furthermore, significant statistical deviation is observed in the pulse power capabilities at higher SOC values (70%–80%) across all three temperatures, with select cells exhibiting broad distributions ranging from 3 W to 7 W.

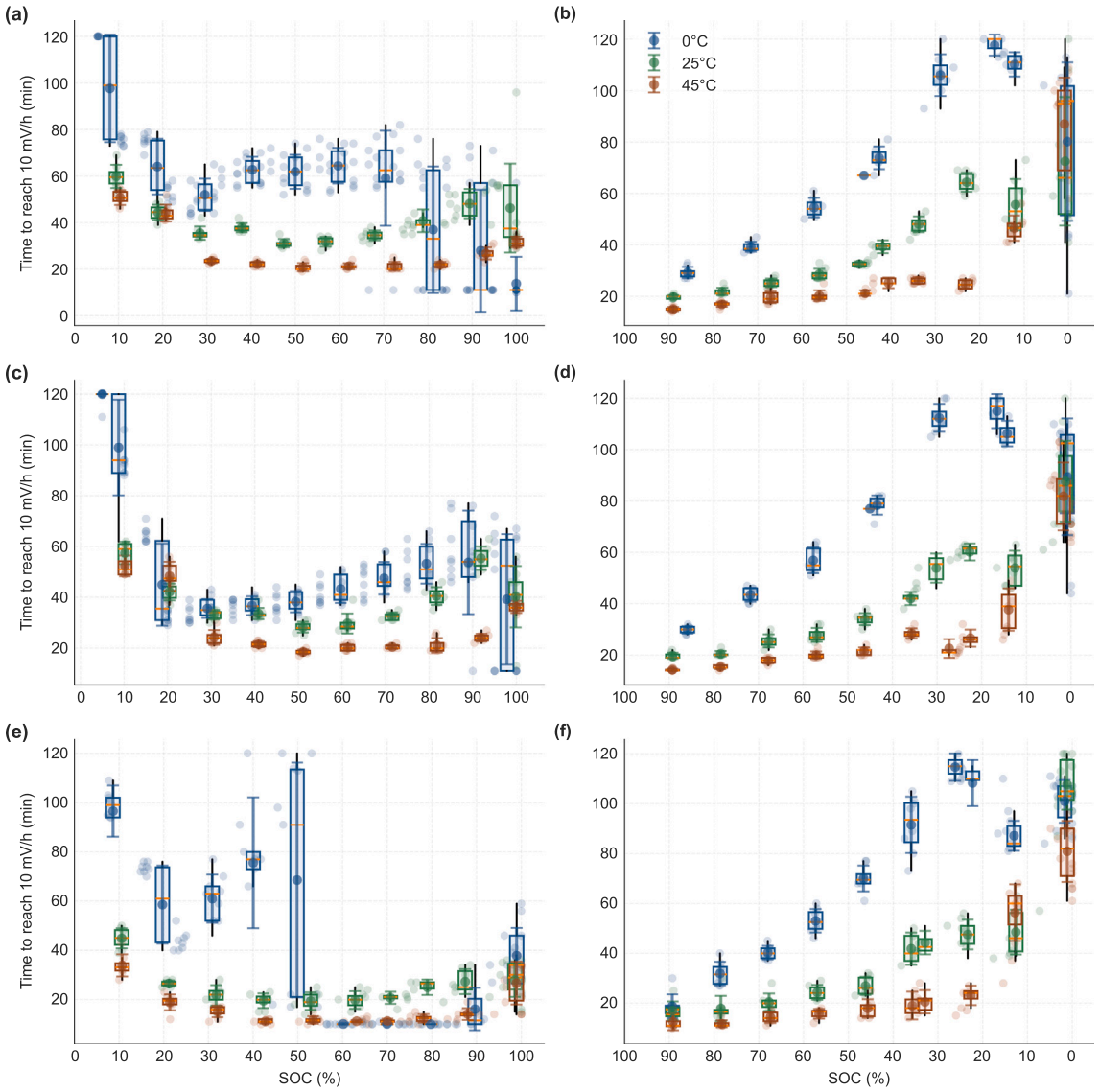


**Fig. 15.** SOC-dependent voltage relaxation time to the $10\,\mathrm{mV\,h^{-1}}$ criterion ($|dV/dt| < 2.8 \times 10^{-6}\,\mathrm{V\,s^{-1}}$) for eight NFM cells after GITT pulses at 1 C, 0.5 C and 0.1 C (rows), during charge (left) and discharge (right). Boxes show IQR with median; markers show mean ±1 SD; dots show individual measurements.

***Remarks:*** Pulse power capability derived from $R_{1s}$ exhibits strong temperature and SOC dependence:

(i) Across 90% to 0% SOC, discharge pulse power spans approximately 7 W to 2 W, with the highest mean values at 45 °C.
(ii) Power capability at 0 °C is substantially reduced relative to 25 °C, with the gap most evident below ~60% SOC.
(iii) Cell-to-cell dispersion is largest at higher SOC (70%–80%) across all temperatures, with values ranging roughly from 3 W to 7 W.

Practically, these statistics translate into temperature- and SOC-dependent power-limits, with extra margin reserved for high-SOC operation.

### 3.4. Voltage relaxation characterisation

Fig. 15 summarises the distribution of relaxation times for NFM required to satisfy the $10\,\mathrm{mV\,h^{-1}}$ criterion ($|dV/dt| < 2.8 \times 10^{-6}\,\mathrm{V\,s^{-1}}$) following each GITT pulse, shown as a function of SOC for 0 °C, 25 °C and 45 °C. Results are grouped by pulse rate (rows) and by charge/discharge direction (left/right); boxes indicate the IQR with median, markers show mean ±1 SD, and dots show individual measurements. Relaxation times are capped at 120 min when the criterion is not achieved within the 2-hour rest.

Voltage relaxation analysis at different C-rates and temperatures reveals that, across all SOC levels, the time to reach the $10\,\mathrm{mV\,h^{-1}}$ criterion depends strongly on temperature, SOC and pulse rate, and is not always achieved within the 2-hour rest under cold and low-SOC conditions (Fig. 15). During charging, relaxation times at 25 °C and 45 °C remain comparatively short through the mid-SOC range yet increase and become more dispersed towards the SOC end-points, with the strongest broadening observed at 0 °C. By contrast, the discharge process shows a clearer SOC dependence, with relaxation times rising sharply and dispersion increasing as SOC decreases, most pronounced at 0 °C where several steps approach the 2-hour limit or reach the 120-min cap. For most GITT steps, the criterion is reached well before the end of the 2-hour rest. Accordingly, we treat the rest-end voltage as a quasi-OCV for SOC–OCV mapping; when the criterion is satisfied, it provides a closer approximation to equilibrium, whereas when it is not satisfied within 2 hours (notably at low SOC and 0°C), residual drift may remain at the end of the rest period.

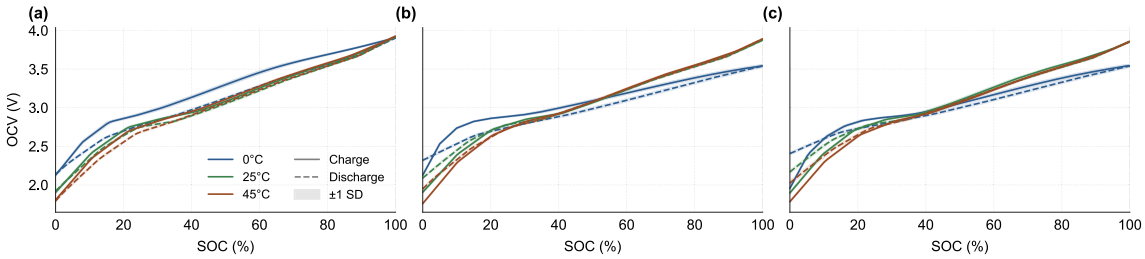


**Fig. 16.** SOC–OCV characteristics of NFM Na-ion cells at (a) 0.1 C, (b) 0.5 C, and (c) 1 C, measured at 0 °C (blue), 25 °C (green), and 45 °C (red). Solid and dashed lines represent the mean charging and discharging curves, respectively. Shaded regions indicate ±1 standard deviation ($n$ = 8).

***Remarks:*** Voltage relaxation times measured via GITT show systematic SOC-, temperature- and rate-dependence:

(i) During charging above ~30% SOC, relaxation times are weakly sensitive to 0 °C and 45 °C, remaining near ~50 s for 1 C and 0.5 C, and near ~25 s for 0.1 C.
(ii) At 25 °C under 1 C and 0.5 C, substantial variability persists up to high SOC (reported up to ~70% SOC).
(iii) During discharge, relaxation time increases as SOC decreases, and low temperature amplifies both the magnitude and the sample-to-sample spread, particularly at low SOC.

These distributions can be used to set temperature- and SOC-dependent rest-time requirements in test protocols and to tune relaxation-aware state estimation.

### 3.5. SOC–OCV characteristics

The SOC during GITT measurements was calculated using coulomb counting method, with the integrated capacity calibrated against the cell's actual capacity determined from the complete charging or discharging sequence of 10% SOC increments. It should be noted that, in the GITT charging tests at 0°C, all cells completed the full 20 steps without reaching the upper voltage cut-off.

The SOC–OCV behaviour of the NFM chemistry is summarised in Fig. 16(a–c), presenting statistical aggregates of eight cells pulsed at 0.1 C, 0.5 C, and 1 C, respectively; detailed individual profiles are provided in Supplementary Fig. S5. Within each C-rate, the statistical mean curves for the three test temperatures (0 °C, 25 °C, and 45 °C) are overlaid. The NFM cells demonstrate robust SOC–OCV consistency with minimal standard deviations. In particular, at 25 °C and 45 °C the charge and discharge SOC-OCV curves remain closely overlapped beyond ~40% SOC, indicating negligible hysteresis in this region.

At elevated temperatures, the SOC–OCV profiles display smoother voltage trajectories across all tested C-rates. This behaviour is consistent with enhanced ion transport and reaction kinetics, which tend to reduce the prominence of plateau-like features in the SOC–OCV curves. In the lower-SOC range, the OCV exhibits a voltage drop at elevated temperatures, a phenomenon consistent with observations in specific Li-ion chemistries [44,45].

By contrast, at 0 °C the charging SOC–OCV curve shows a clear change in slope around ~20% SOC. The voltage increases more steeply below this level and then transitions to an approximately linear rise through the mid-SOC range. The discharging SOC–OCV curve exhibits a weaker feature near ~20% SOC, such that the charge–discharge separation becomes asymmetric in the low-to-mid SOC region.

Furthermore, across 0.1 C to 1 C, the overall SOC–OCV signature is preserved, while rate-dependent smoothing of the low-SOC feature on the discharging curve is observed at 0 °C. This suggests that the 2-hour rest period yields stable OCV extraction for the main features, although additional relaxation may be required to fully resolve low-temperature,

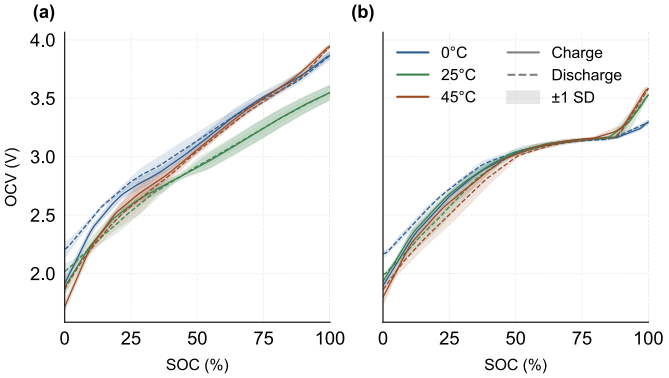


**Fig. 17.** Statistical comparison of SOC-OCV characteristics for (a) CFM and (b) NFPP Na-ion cells across three operating temperatures: 0 °C (blue), 25 °C (green), and 45 °C (red). Solid lines represent mean charging curves and dashed lines represent mean discharging curves. Shaded regions indicate ±1 standard deviation ($n$ = 3 cells per condition).

low-SOC nuances at the higher pulse rates. This observation is broadly consistent with the trends seen in Fig. 15.

For the CFM chemistry (Fig. 17a), relatively large standard deviations are observed across the tested samples at all three temperatures, indicating greater cell-to-cell variability. While charge–discharge hysteresis is minimal at higher SOC levels, the OCV characteristics show pronounced variation between temperatures. This high thermal sensitivity presents a substantial challenge for developing robust, temperature-adaptive SOC estimation algorithms.

In NFPP cells (Fig. 17b), good consistency and low hysteresis are maintained primarily within the 50%–80% SOC range. Outside this window, at both lower and higher SOC levels, inter-cell consistency deteriorates, and temperature-induced divergence becomes increasingly significant. The detailed SOC-dependent OCV profiles for the tested CFM and NFPP cells are presented in Supplementary Figs. S6 and S7, respectively.

***Remarks:*** SOC–OCV characteristics are chemistry- and temperature-dependent and have implications for robust SOC estimation.

(i) For NFM ($n$ = 8), the SOC–OCV curves show minimal dispersion; at 25 °C and 45 °C the charging and discharging SOC–OCV curves are nearly coincident beyond ~40% SOC, indicating negligible hysteresis in this region.
(ii) For NFM, the overall SOC–OCV signature is preserved across 0.1 C, 0.5 C and 1 C under the present 2-hour relaxation protocol; however, at 0 °C a modest rate-dependent smoothing of the low-SOC feature is observed, suggesting that additional relaxation may be beneficial to better characterise the low-SOC behaviour at low temperature at the higher pulse rates.
(iii) The reference chemistries show larger variability ($n$ = 3 per condition). CFM exhibits comparatively large dispersion and

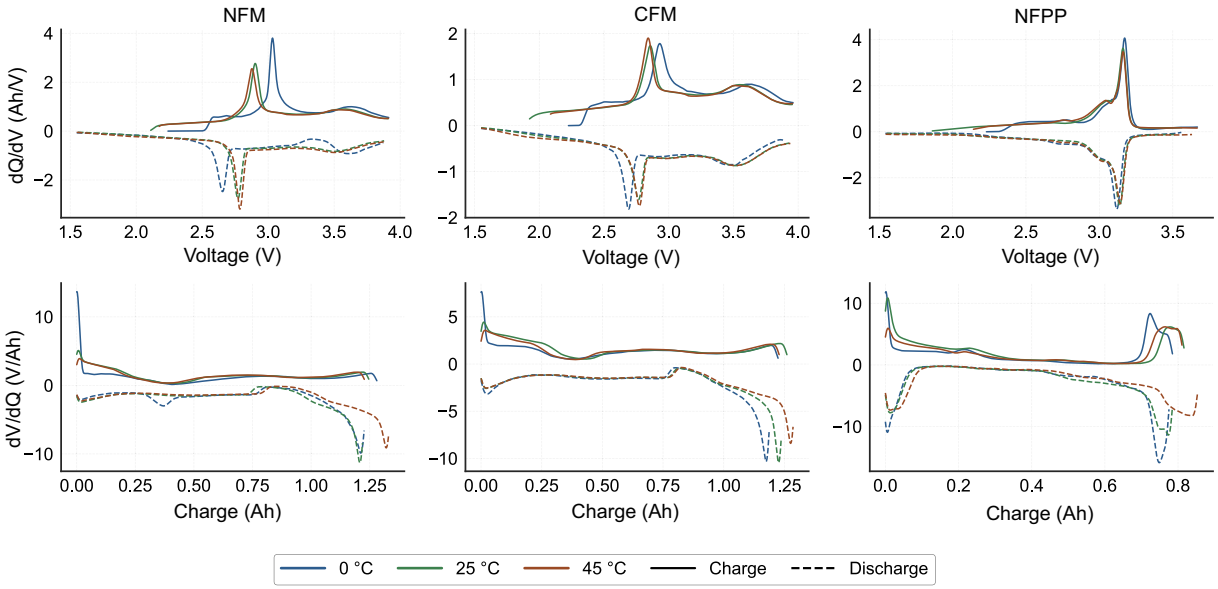


**Fig. 18.** Incremental capacity (top row) and differential voltage (bottom row) profiles of NFM, CFM and NFPP cells measured at 0 °C, 25 °C and 45 °C under 0.1 C galvanostatic cycling. Solid and dashed lines correspond to charge and discharge, respectively.

stronger temperature sensitivity, whereas NFPP is most consistent primarily within the mid-SOC window (50%–80% SOC).

These results motivate chemistry-specific OCV maps and temperature-dependent hysteresis handling in SOC observers.

### *3.6. Incremental capacity and differential voltage characteristics at different temperatures*

Fig. 18 compares the temperature-dependent ICA and DVA signatures of three sodium-ion chemistries from the 0.1 C voltage–capacity profiles at 0, 25 and 45 °C. The two layered oxide cells (NFM and CFM) display broadly similar ICA and DVA fingerprints, consistent with comparable sequences of electrochemical processes despite differences in composition. By contrast, NFPP exhibits a more localised incremental capacity response, with a dominant feature concentrated within a narrower voltage window, reflecting a more confined distribution of incremental capacity.

A consistent temperature dependence is observed for all three cells. At 0 °C, the main dQ/dV features during charge shift to higher voltages, while the corresponding discharge features shift to lower voltages. This bidirectional displacement widens the separation between charge and discharge features and indicates greater voltage hysteresis at low temperature. The widening is more evident for the layered oxide cells, pointing to a stronger low-temperature dependence of their voltage hysteresis.

The evolution of peak intensity further differentiates the chemistries. Given that ICA peak intensity can be influenced by polarisation as well as by the differentiation and smoothing procedure, intensity comparisons are interpreted qualitatively and primarily within each chemistry. Within this context, NFM and NFPP exhibit higher maximum dQ/dV intensities at 0 °C than at 25 °C and 45 °C, consistent with a larger fraction of capacity being exchanged over a narrower apparent voltage interval under cold conditions. In contrast, CFM shows comparable peak magnitudes across all three temperatures, with temperature effects expressed mainly as modest shifts in feature position rather than substantial changes in peak intensity.

The DVA profiles corroborate the temperature-dependent changes observed in the ICA curves. For the layered oxide cells, the charge dV/dQ curves overlap closely over much of the mid-capacity region, whereas greater divergence appears near the beginning of charge and towards the end of discharge. A similar behaviour is observed for NFPP, with partial overlap over intermediate capacity intervals and increasing separation outside these regions. The ICA peak separation and the segmented DVA divergence indicate that low temperature primarily affects the charge–discharge separation and the measured voltage response, particularly near the boundaries of the operating window, while the ordering of the dominant features is broadly preserved.

***Remarks:*** ICA/DVA features remain ordered across temperature but exhibit systematic charge–discharge separation at low temperature:

(i) The layered oxide cells (NFM and CFM) show broadly similar ICA/DVA fingerprints, whereas NFPP exhibits a more localised incremental-capacity response within a narrower voltage window.
(ii) At 0 °C, dQ/dV features shift to higher voltages on charge and to lower voltages on discharge, widening charge–discharge separation; the effect is more evident for the layered oxides.
(iii) Low-temperature effects are most visible near the operating-window boundaries in DVA, while dominant mid-capacity features remain present across 0–45 °C.

Because these features are repeatable and temperature-sensitive, they can be used as diagnostics to track model parameters, without attributing them to specific electrodes.

### *3.7. Casing strain response during cycling*

The temperature-compensated strain responses are strongly correlated with the voltage profile during both 0.5 C and 0.1 C cycling for two NFM cells instrumented in the axial and circumferential configurations, respectively (Fig. 19). The two sensor orientations exhibit distinct trends. In the axial configuration, strain is predominantly out of phase with voltage at 0.5 C (i.e., decreasing during charge and increasing during discharge), whereas at 0.1 C it is largely in phase with voltage. In contrast, the circumferential configuration shows a more structured, voltage-synchronous profile, with strain increasing during charging and decreasing during discharging.

At 25 °C and 0.1 C, the axial and circumferential configurations show comparable strain amplitudes, whereas the 0.5 C condition produces substantially larger casing-strain excursions (Fig. 19b,e). This indicates

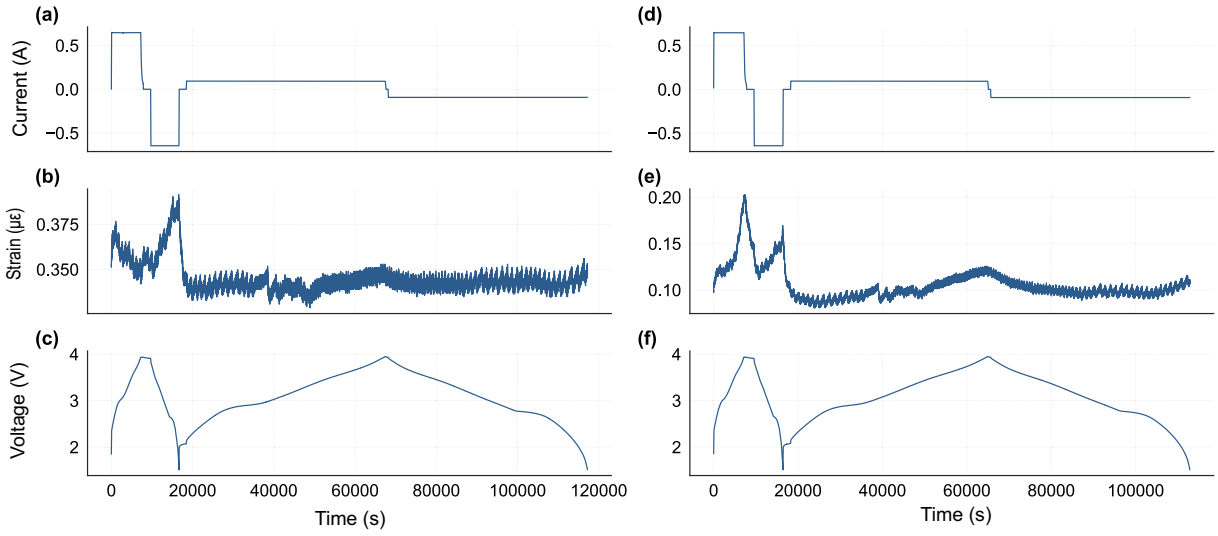


**Fig. 19.** Synchronised current, FBG-measured casing strain, and voltage during 0.5 C and 0.1 C cycling of NFM cells. Axial sensor configuration (a–c) and circumferential configuration (d–f). Current (a,d), strain (b,e), and voltage (c,f).

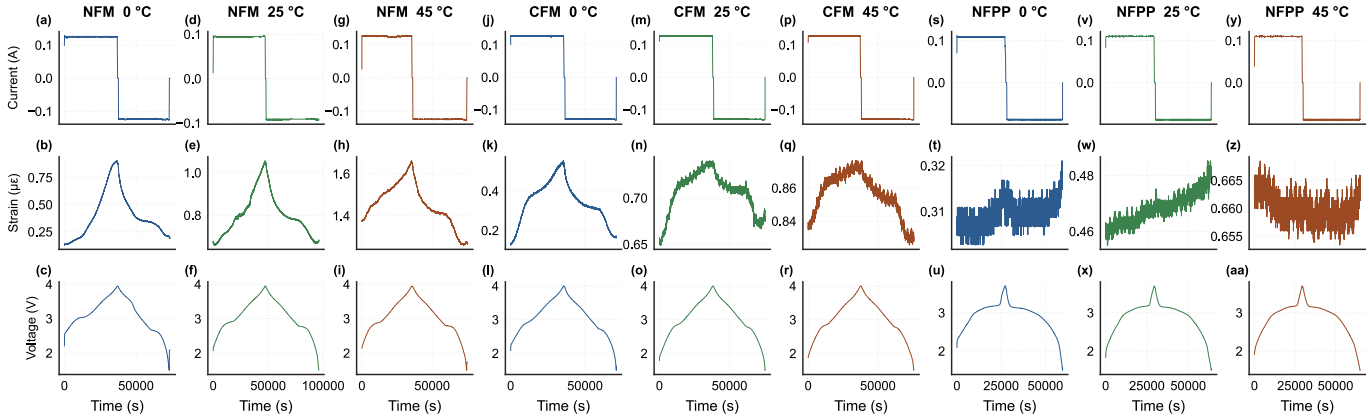


**Fig. 20.** Synchronised current, voltage, and circumferential casing strain of NFM, CFM, and NFPP cells measured at 0 °C, 25 °C, and 45 °C under 0.1 C cycling.

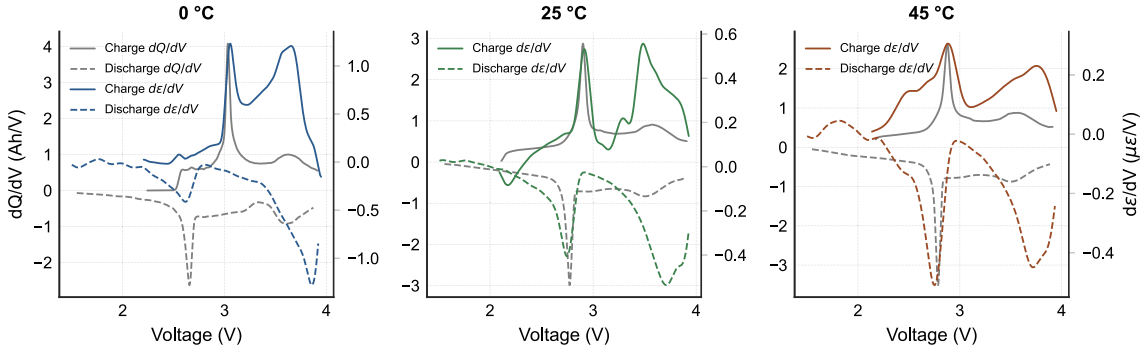


**Fig. 21.** Differential strain response (d$\varepsilon$/dV) of the NFM cell measured at 0 °C, 25 °C, and 45 °C under 0.1 C cycling. The corresponding incremental capacity (dQ/dV) profiles are shown for reference.

a pronounced rate dependence of the measured casing-strain response under the present measurement setup.

Using the circumferential configuration, NFM, CFM, and NFPP cells were cycled at 0.1 C at 0 °C, 25 °C, and 45 °C (Fig. 20). The layered-oxide cells (NFM and CFM) exhibit cycle-synchronous, predominantly reversible casing-strain variations at all three temperatures, and the principal features remain aligned with the charging and discharging voltage profiles. Higher temperatures tend to shift the baseline and the overall strain magnitude, while the shape of the strain profile is broadly retained. In contrast, the NFPP cell shows no discernible cycle-synchronous casing-strain signal within the resolution of the present casing-mounted measurement across 0 °C–45 °C.

Fig. 21 compares d$\varepsilon$/dV with dQ/dV for the NFM cell across 0 °C–45 °C, obtained using the same data-processing procedure. The

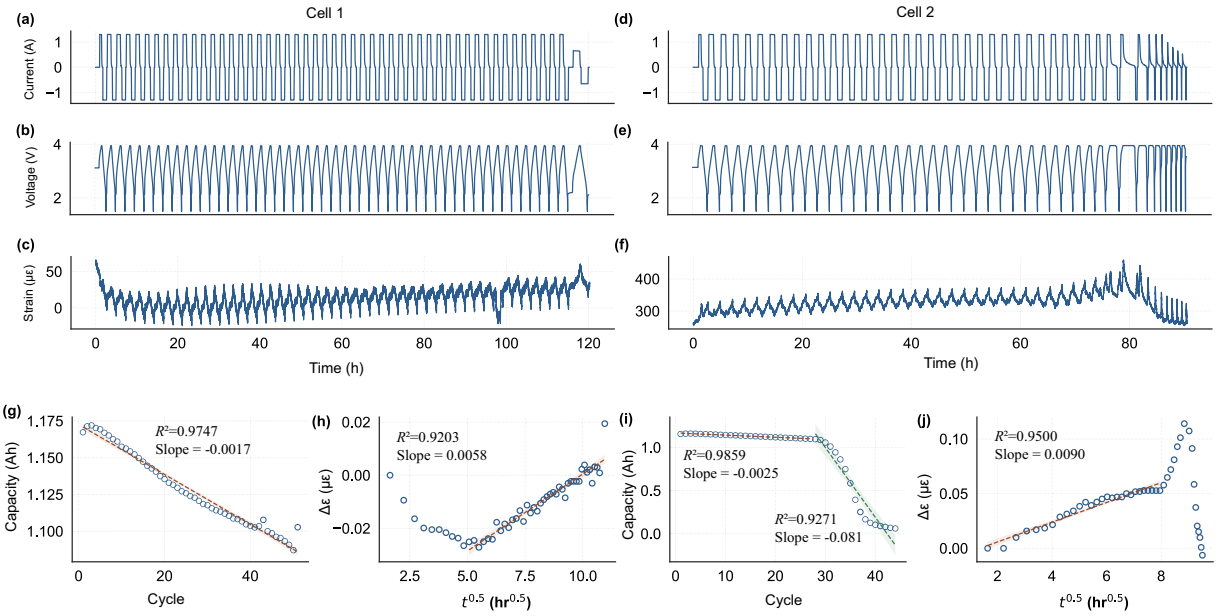


**Fig. 22.** Comparative analysis of two cells cycled under a 1 C current profile, using CC-CV charging and CC discharging conditions over 50 cycles. (a), (b), and (c) present the current, voltage, and strain variations for Cell 1, respectively, while (d), (e), and (f) show the corresponding data for Cell 2. (g) and (i) depict the capacity fade as a function of cycle number for Cell 1 and Cell 2, respectively. (h) and (j) display the cumulative residual strain increment, $\Delta\varepsilon_{cum}$, plotted against the square root of cycling time for Cell 1 and Cell 2, respectively.

dominant $d\varepsilon/dV$ features coincide with the main dQ/dV peaks at each temperature, indicating that the most rapid changes in casing strain occur in the principal charge-storage regions identified electrochemically. Temperature alters the sharpness and breadth of these features, with more localised responses at 0 °C and broader responses at 45 °C.

***Remarks:*** FBG measurements reveal orientation-, rate- and chemistry-dependent casing-strain observability:

(i) For NFM, casing-strain excursions are substantially larger at 0.5 C than at 0.1 C under otherwise identical conditions, indicating strong rate dependence.
(ii) Sensor orientation matters, as the axial and circumferential configurations exhibit different strain–voltage trends; therefore, consistent placement is required for cross-test comparability.
(iii) Using circumferential sensing, layered oxides (NFM, CFM) show clear cycle-synchronous strain signatures across 0 °C–45 °C, whereas NFPP shows no discernible casing-level signature under the present casing-mounted geometry.

In other words, this indicates when casing-level strain sensing is informative for control and monitoring, and when the signal is likely unobservable under the chosen mounting configuration.

### 3.8. Progression of irreversible strains and analysis of capacity fade

The electrochemical–mechanical evolution of the two NFM cells during repeated cycling is summarised in Fig. 22. Both cells exhibited distinct cycling behaviours, with Cell 1 successfully completing all 50 prescribed cycles while Cell 2 terminated prematurely after 45 cycles. Analysis of the current and voltage profiles revealed remarkably consistent characteristics for both cells through the first ~30 cycles, after which Cell 2 began to display incomplete cycling profiles. Of particular interest were the strain profiles, which demonstrated notable differences in both pattern and magnitude throughout the entire cycling procedure. Cell 1 exhibited a characteristic reduction in strain during the initial cycles. This behaviour is likely attributable to early-cycle mechanical settling and progressive alleviation of internal stresses during (de)sodiation, which collectively reduce the net casing-level stress response and support more stable cycling [46].

Concurrently, the evolution of the CEI, progressive growth of the SEI layer, electrolyte decomposition at the electrode surface, and irreversible structural modifications are known to contribute to residual deformation accumulation during cycling [47,48]. The net effect of these phenomena is a gradual deterioration of the electrode's structural integrity, which is consistent with the observed capacity fade, with a fade rate of $1.70 \times 10^{-3}$ Ah cycle$^{-1}$ as illustrated in Fig. 22(g). The cumulative residual strain increment evolution resulting from these degradation mechanisms is evident in Fig. 22(h), where Cell 1 demonstrates an initial phase of strain adaptation followed by stabilisation.

Cumulative residual strain is often analysed as a function of $\sqrt{t}$, and prior work has reported an approximately linear dependence in this representation, with contributions from interfacial and diffusion-limited degradation processes [49,50]. Using the same representation here, Cell 1 displays a clear linear $\Delta\varepsilon_{cum}$–$\sqrt{t}$ region from approximately $5\,h^{1/2}$ onwards.

This temporal region demonstrates a substantial positive correlation ($R^2 = 0.920$), quantified by a slope of $5.79 \times 10^{-3}$ $\mu\varepsilon\,h^{-1/2}$ in the linear regression analysis. Because $\Delta\varepsilon_{cum}$ is computed as an absolute residual-strain increment, the fitted slope is reported on a consistent physical scale and is not artificially inflated by normalisation to a near-zero baseline, enabling direct cross-cell comparison.

In contrast, Cell 2 exhibits predictable strain variation patterns throughout the first ~30 cycles (as shown in Fig. 22(f)), consistent with previous reports [49,50]. The casing strain response is substantial during the initial cycle and then progressively decreases with further cycling [46]. Moreover, the strain magnitude for Cell 2 is considerably higher than that for Cell 1, which arises from variations in electrode thickness, active material loading, and assembly inconsistencies (e.g., uneven pressure application or misalignment) [51].

Additionally, Cell 2 exhibits a clear linear relationship ($R^2 = 0.950$) from the onset of cycling up to approximately $8\,h^{1/2}$, corresponding to the first ~30 stable cycles, as shown in Fig. 22(j). The slope ($9.04 \times 10^{-3}$ $\mu\varepsilon\,h^{-1/2}$) is modestly higher than that of Cell 1 within its linear

window, whereas the capacity fade rate is higher, with an early-stage fade rate of $2.49 \times 10^{-3}$ Ah cycle$^{-1}$ up to cycle 27 and a pronounced terminal decay of $8.06 \times 10^{-2}$ Ah cycle$^{-1}$ beyond cycle 27 (as shown in Fig. 22(i)).

Beyond the first 30 stable cycles, a significant increase in cumulative residual strain increment indicates the activation of additional degradation mechanisms. These mechanisms are primarily associated with mechanical instabilities, such as cracking and delamination, which stem from repeated volume changes and are exacerbated when thick or inhomogeneous CEI layers develop, leading to uneven stress distributions across the cathode surface [48,52]. After reaching a maximum around cycle 37, $\Delta\varepsilon_{cum}$ declines sharply and can become negative. Small negative excursions of $\Delta\varepsilon_{cum}$ may reflect baseline drift and thermo-mechanical coupling in casing-level measurements rather than a true reversal of irreversible deformation. Therefore, the linear windows and the pre-failure growth trend are used as the primary comparative metrics.

***Remarks:*** Medium-term 1 C cycling shows that irreversible casing strain evolves alongside capacity fade, but trajectories differ substantially between nominally identical cells:

(i) Cell 1 completes 50 cycles, whereas Cell 2 terminates at 45 cycles; divergence emerges after ~30 stable cycles when Cell 2 begins to show incomplete profiles.
(ii) Capacity fade rates are on the order of $10^{-3}$ Ah cycle$^{-1}$ during the stable stage ($1.70\times10^{-3}$ for Cell 1; $2.49\times10^{-3}$ for Cell 2 up to cycle 27), followed by a rapid terminal decay for Cell 2 ($8.06\times10^{-2}$ Ah cycle$^{-1}$ beyond cycle 27), accompanied by continued evolution of $\Delta\varepsilon_{cum}$.
(iii) $\Delta\varepsilon_{cum}$ exhibits an approximately linear dependence on $\sqrt{t}$ over extended windows ($R^2 = 0.920$ for Cell 1 beyond ~5 h$^{1/2}$ with slope $5.79\times10^{-3}$ $\mu\varepsilon$ h$^{-1/2}$; $R^2 = 0.950$ for Cell 2 up to ~8 h$^{1/2}$ with slope $9.04\times10^{-3}$ $\mu\varepsilon$ h$^{-1/2}$), with Cell 2 showing a marked increase after ~30 cycles.

Casing-level residual strain thus provides an additional measurable health signal that can complement capacity-based indicators for condition monitoring and control supervision.

### 3.9. Cycling performance and ageing signatures

Fig. 23 shows the SOH trajectories of the five tested Na-ion cells during long-term cycling. The NFM cells (NFM-1 and NFM-2, from two different production batches) exhibit rapid capacity fade, with a decay

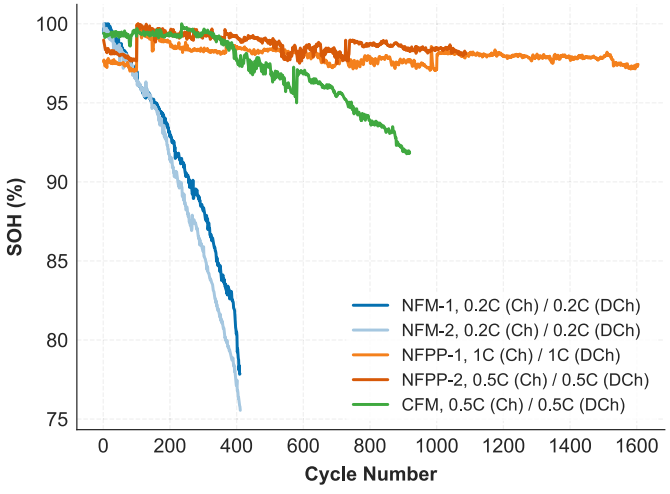


**Fig. 23.** SOH evolution of Na-ion cells with different cathode materials at the indicated C-rates during long-term cycling.

behaviour that can be approximated by a power-law trend from the onset of cycling until approximately 80% SOH (Supplementary Fig. S8). The CFM cell demonstrates moderate stability, retaining over 93% SOH after 800 cycles. In contrast, the NFPP cells show exceptional capacity retention. After an initial equilibration over the first 100 cycles, the accessible discharge capacity slightly increases and then remains nearly constant over extended cycling.

The long-term cycling behaviour of the investigated Na-ion cells is summarised in Fig. 24. Panels (a,d,g,j,m) show the charge–discharge voltage–capacity profiles, while the corresponding incremental-capacity (ICA, dQ/dV) and differential-voltage (DVA, dV/dQ) curves are presented in (b,e,h,k,n) and (c,f,i,l,o), respectively. The colour scale represents cycle progression, with lighter shades corresponding to early cycles and darker shades to later cycles. In the ICA and DVA panels, the upper and lower branches correspond to the charging and discharging segments of the RPTs, respectively, and arrows with labels indicate the shift direction of selected features of interest (FOIs) during cycling.

Both NFM cells cycled at 0.2 C show highly consistent voltage–charge evolution, with the cut-off voltages being reached at progressively lower capacity as cycling proceeds (Figs. 24a,d). In the corresponding ICA curves (Figs. 24b,e), the feature onset (FOI (i)) during charging shifts slightly towards higher voltages, accompanied by a gradual decrease in peak amplitude. The dominant peak (FOI (ii)) remains clearly discernible throughout cycling, while the voltage corresponding to its maximum intensity also shifts to higher values. It is noted that peak broadening can shift the apparent voltage of maximum intensity without necessarily implying a change in the underlying redox potential [53]. During discharge, the main negative feature (FOI (ii′)) progressively weakens, with only limited displacement in voltage. In parallel, the high-voltage shoulder becomes less pronounced, consistent with an overall broadening of the differential response as cycling proceeds.

The DVA traces (Figs. 24c,f) indicate that the most pronounced evolution with cycling occurs near the ends of the capacity window, whereas changes in the mid-capacity region are more gradual. The same localisation is retained when dV/dQ is replotted against normalised SOC (Supplementary Fig. S9). As ICA and DVA interpretations are chemistry dependent, the trends are discussed here at a phenomenological level; attribution to specific degradation modes would require electrode matching and complementary diagnostics [53].

The CFM cell cycled at 0.5 C retains a broadly similar voltage–charge profile to the NFM cells, characterised by a comparable sloping behaviour within the fixed voltage window (Fig. 24g). The corresponding ICA response (Fig. 24h) exhibits distinct primary peaks that persist throughout cycling, with no evident emergence or disappearance of features. During charge, both the feature onset (FOI (i)) and the peak maximum (FOI (ii)) shift slightly towards higher voltages. During discharge, the high-voltage feature (FOI (iii′)) shows only marginal voltage displacement, accompanied by minimal attenuation. When replotted as a function of normalised SOC (Supplementary Fig. S9), the DVA traces largely overlap across most of the SOC range. A modest shift towards lower SOC is observed for the discharge branch in the mid-SOC region, while minor scatter appears near the charge and discharge cut-offs.

In contrast, the NFPP cells cycled at 1 C and 0.5 C exhibit a distinct voltage and differential signature compared with the NFM and CFM cells (Figs. 24j–o). Although neither cell reaches the manufacturer-rated capacity within the tested voltage window, the voltage–charge profiles remain closely overlapped across most of the cycling period (Figs. 24j,m). The corresponding ICA traces obtained from periodic RPTs (Figs. 24k,n) likewise show a high degree of overlap. The onset feature (FOI (i)) remains essentially unchanged with cycling for both cells. The peak maximum (FOI (ii)) exhibits a slight reduction in amplitude without a discernible shift in voltage, whereas the corresponding discharge-branch trough (FOI (ii′), defined by the minimum in dQ/dV) shows only a small increase in magnitude and no systematic voltage

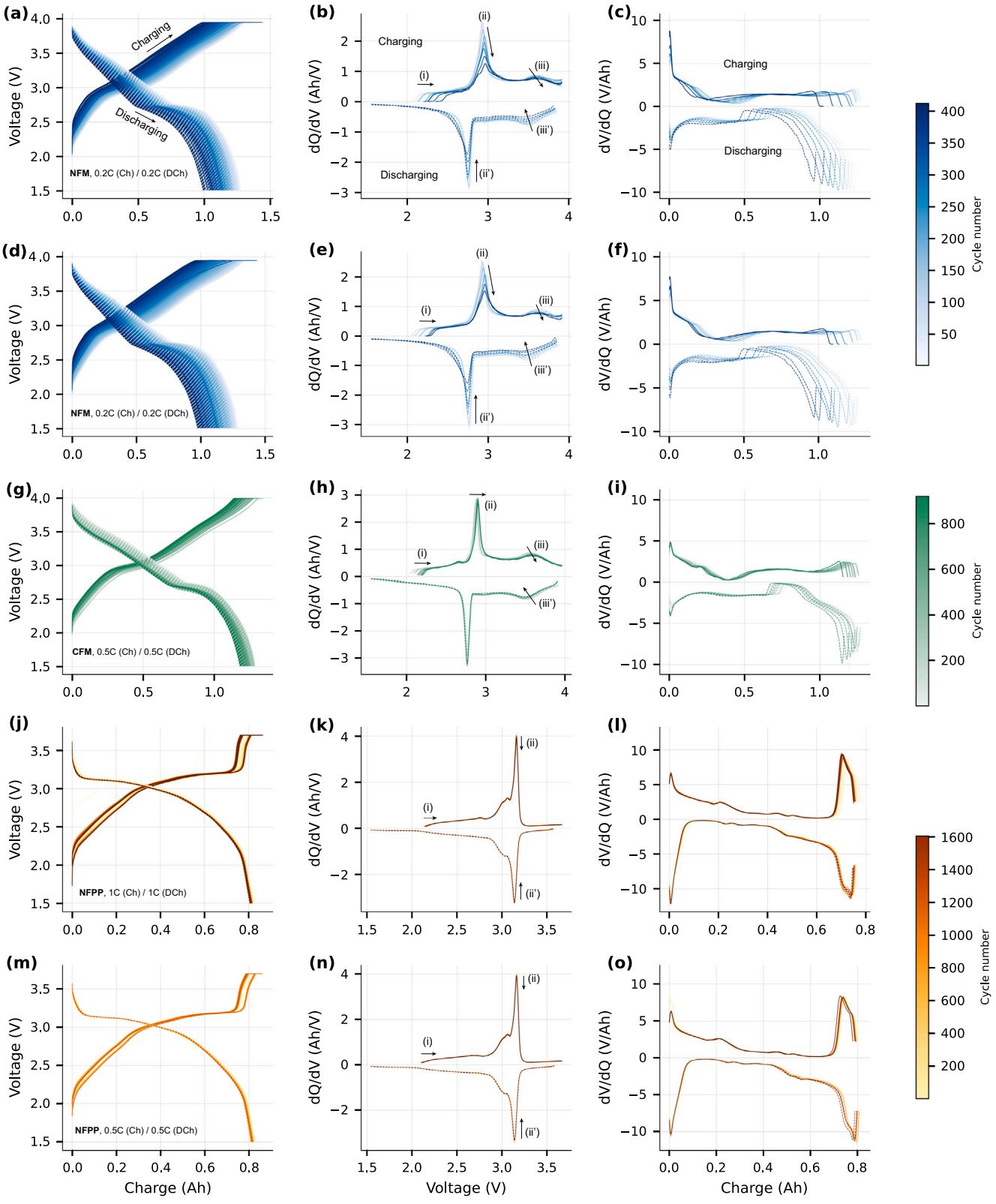


**Fig. 24.** Cycling voltage profiles and differential analyses of five Na-based cells (colour intensity increases with cycle number).

displacement. Compared with the NFM and CFM cells, the voltage separation between the charge-branch peak maximum and the corresponding discharge-branch trough is smaller for the NFPP cells. The DVA profiles plotted against charge (Figs. 24l,o) indicate that the most pronounced variations with cycling are confined to the cut-off regions. In particular, the primary charge-side DVA peak shifts towards lower capacity, while the response immediately preceding the cut-off remains largely invariant. When replotted as a function of normalised SOC (Supplementary

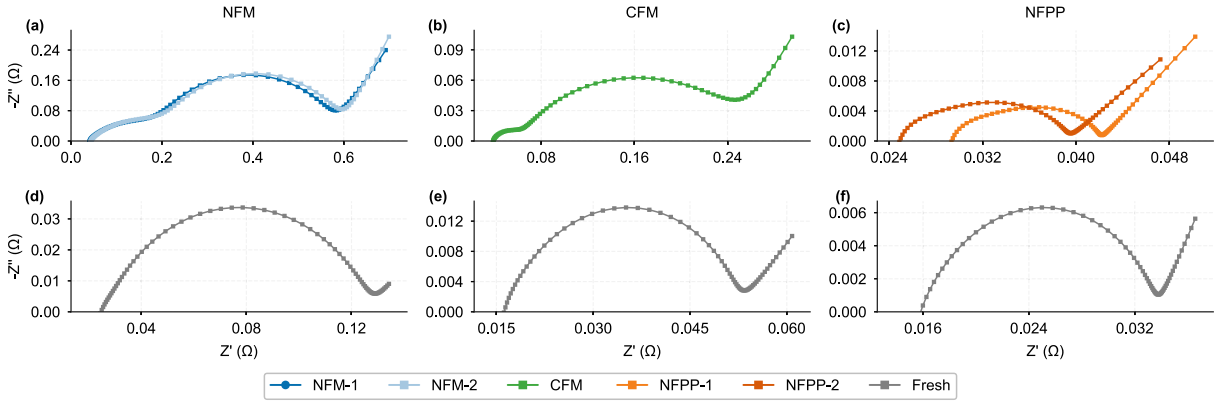


**Fig. 25.** Nyquist plots of aged and fresh (grey) Na-ion cells for NFM, CFM and NFPP chemistries; aged spectra are shown in cell-specific colours.

Fig. S9), the charge-branch DVA peak shifts towards higher SOC and increases in magnitude, accompanied by a slight contraction of the discharge-branch dV/dQ values at high SOC.

Fig. 25 compares the Nyquist response of fresh and aged Na-ion cells for each chemistry, with aged spectra shown in the top row and the corresponding fresh spectra in the bottom row. All spectra were measured at 25 °C and 50% SOC over a frequency range of 10 kHz to 0.01 Hz. Across all three chemistries, ageing is accompanied by an overall increase in the impedance response, with a larger high-to-mid-frequency arc in the aged spectra. This change is most pronounced for the NFM cells, more moderate for the CFM cell, and comparatively limited for the NFPP cells. These impedance trends are consistent with the voltage–capacity and differential analyses discussed above. In particular, the larger impedance growth observed for the NFM cells aligns with the more pronounced peak broadening and evolution of ICA/DVA features, whereas the relatively minor impedance change in the NFPP cells is compatible with the high stability of their differential signatures. Within the measured frequency window, no new low-frequency feature emerges that would suggest a qualitative shift towards a newly dominant diffusion-limited response in the aged spectra. It is emphasised that the EIS results provide a complementary, system-level perspective on cycling-induced polarisation rather than a direct attribution of individual ICA or DVA features to specific electrochemical processes. Nevertheless, the consistent trends across impedance and differential analyses support the view that the observed evolution of differential features is influenced by the concomitant rise in impedance (polarisation) during cycling.

***Remarks:*** Long-term cycling highlights strong chemistry dependence in capacity retention and ageing signatures under fixed operating windows:

(i) NFM cells (0.2 C) show rapid capacity fade that follows an approximate power-law trend down to ~80% SOH, whereas the CFM cell retains >93% SOH after 800 cycles and NFPP cells show near-constant capacity after an initial ~100-cycle equilibration.
(ii) Periodic RPT-based ICA/DVA features remain reproducible within each chemistry and evolve differently across NFM, CFM and NFPP, enabling compact tracking metrics even without electrode-resolved diagnostics.
(iii) Fresh–aged EIS at 25 °C and 50% SOC shows impedance growth across all chemistries, most pronounced for NFM and least for NFPP, consistent with the relative severity of differential-feature evolution.

The combined voltage–differential–impedance evidence supports chemistry-specific ageing models and feature selection for monitoring and control-oriented diagnostics.

## 4. Discussion

This work presents characterisation results focusing on attributes directly actionable for the system-level management of sodium-ion cells. It centres on quantifying the representative characteristics and cell-to-cell dispersion of early-generation commercial layered-oxide NFM cells. To examine the generality and transferability of the observed behaviours from these NFM cells, specific attributes are benchmarked against an additional early-stage commercial layered-oxide chemistry (CFM), a different cathode technology based on a polyanion chemistry (NFPP), and mature lithium-ion cells (LFP and NCA). The comparisons cover low-temperature capacity retention, HPPC voltage response, temperature-dependent impedance (measured from −30 °C–45 °C), temperature-related SOC–OCV relationships (at 0 °C, 25 °C and 45 °C), mechanical casing-strain (at 0 °C, 25 °C and 45 °C), and ageing signatures. These comparisons distinguish between universal battery behaviours, limitations inherent in early-commercial Na-ion cells, and traits specific to the NFM chemistry. This distinction identifies which constraints, OCV maps and resistance metrics can be transferred across chemistries and which require chemistry-specific calibration for Na-ion state estimation and control. Table 4 summarises the key characterisation outcomes and system-level control implications identified in this work.

### 4.1. Temperature and chemistry dependence under aligned protocols

Analogous to Li-ion batteries, the Na-ion cells evaluated herein exhibit increased polarisation and reduced usable capacity as temperature decreases. Specifically, under the applied protocol, all chemistries yielded reduced discharge capacities at −20 °C relative to 25 °C, while impedance spectra exhibit an enlarged mid-frequency polarisation feature at lower temperature. Inter-cell consistency among replicates is highest at 25 °C, whereas it degrades at 45 °C and under low-temperature conditions (0 °C to −30 °C) in the present EIS measurements, consistent with the amplification of cell-to-cell variability under rate-limited operation. Despite these shared thermal penalties, an operability contrast emerges under severe sub-zero conditions. While the Li-ion reference cells did not sustain discharge sufficiently to yield a measurable capacity at −40 °C under the present protocol, all three Na-ion chemistries retained measurable capacity, corresponding to 51%–62% of the 25 °C value. At −20 °C, the Na-ion cells also show higher capacity retention than the Li-ion cells (87%–90% versus 72%–75%), demonstrating stronger low-temperature operability for the Na-ion chemistries under the present protocol.

Contrasts between layered-oxide (NFM, CFM) and polyanion (NFPP) Na-ion chemistries are evident under the present protocols across differential features, temperature sensitivity, and casing-strain observability.

**Table 4**
Summary of key characterisation outcomes and system-level control implications derived in this work.

| Implications | Key Characterisation Finding | System-level Implication |
|---|---|---|
| **Sub-zero Operability** | *Comparison:* Na-ion chemistries retained 51%–62% capacity at −40 °C, whereas Li-ion benchmarks failed to sustain discharge.<br>*Kinetics:* All cells followed Arrhenius impedance scaling, but layered oxides (NFM/CFM) showed higher sensitivity ($E_a \approx 70$–$75\,\mathrm{kJ\,mol^{-1}}$) than NFPP. | *Strategy:* Extension of BMS discharge envelopes for Na-ion into severe cold regions inaccessible to Li-ion.<br>*Requirement:* Chemistry-specific thermal derating maps; active pre-heating is likely required for layered oxides to enable power availability. |
| **Charging Supervision** | *Dispersion:* NFM population ($n = 33$) exhibited a heavy-tailed distribution of CV-phase duration ($> 1000$ min outliers) at 0 °C, contrasting with clustering at 25 °C.<br>*Mechanism:* Low-temperature kinetic bottlenecks amplify intrinsic manufacturing heterogeneity. | *Strategy:* Avoidance of fixed voltage-based termination for cold fast-charging.<br>*Requirement:* Adaptive end-of-charge logic incorporating time-domain constraints (e.g., max CV duration) and dispersion-aware balancing. |
| **Power Capability** | *Pulse Response:* NFM displayed pronounced time-dependent polarisation (dynamic) under HPPC, contrasting with the instantaneous (ohmic) drop of NCA.<br>*Resistance:* Pulse-derived resistance ($R_{\mathrm{pulse}}$) significantly exceeded $R_{\mathrm{EIS}}$ at low temperature(s) environment and showed strong SOC dependence. | *Strategy:* Calibration of Power Limits ($P_{\max}$) matched to the specific actuation horizon (1–10 s) rather than frequency-domain impedance metrics.<br>*Requirement:* Explicit modelling of polarisation build-up for NFM; restriction of EIS metrics to offline diagnostics. |
| **State Estimation (SOC)** | *Hysteresis:* Layered oxides (NFM/CFM) showed distinct low-SOC ($< 20\%$) hysteresis and charge–discharge separation at 0 °C.<br>*Relaxation:* GITT equilibration times exhibit significant low temperature variability, complicating OCV capture. | *Strategy:* Implementation of temperature-indexed, chemistry-specific OCV inversion maps.<br>*Requirement:* Propagation of measured OCV dispersion into SOC confidence bounds; dynamic relaxation thresholds. |
| **Feature Observability** | *Mechanical:* Robust voltage-synchronous casing strain detected in NFM/CFM across 0–45 °C; no resolved signal in NFPP.<br>*Differential:* ICA/DVA signatures in layered oxides shift systematically with temperature, maintaining feature identifiability. | *Strategy:* Casing-strain sensing can serve as an additional observable for layered oxides only.<br>*Requirement:* Use of differential features (ICA peaks) for parameter tracking, provided temperature shifts are compensated. |
| **Ageing Diagnostics** | *Degradation:* NFM showed rapid capacity fade and EIS impedance increase; NFPP exhibited exceptional stability.<br>*Mechanism:* Irreversible casing strain follows $\sqrt{t}$ kinetics and correlates linearly with capacity fade in NFM. | *Strategy:* Multi-modal SOH estimation combining electrochemical (impedance rise) and mechanical (residual strain) signals.<br>*Requirement:* Phenomenological ageing models parameterised strictly for the specific chemistry; no cross-chemistry model transfer. |

NFM and CFM display broadly similar ICA and DVA fingerprints, characterised by a systematic low-temperature displacement of charge and discharge features. Under the present casing-mounted circumferential configuration, the layered-oxide cells exhibit clear cycle-synchronous casing-strain signatures similar to the NCA reference cell, whereas NFPP shows no resolved cycle-synchronous casing-strain signature within the measurement resolution. Arrhenius fits of the EIS-derived polarisation resistance further differentiate the chemistries. CFM exhibits the highest temperature sensitivity, while NFPP shows a more moderate dependence, consistent with chemistry-dependent limitations governing polarisation across the measured range.

Beyond the chemistry-level distinctions discussed above, NFM exhibits distinctive kinetic constraints and degradation trajectories. Normalised HPPC pulse responses at 25 °C show that NFM has the largest total voltage drop at 1 C and the largest within-pulse voltage decay over a 10 s pulse, consistent with a drift-dominated polarisation build-up beyond the first 0.1 s sample that is directly relevant to power control. This observation aligns with the impedance spectra measured from −30 °C to 45 °C, where NFM shows the most pronounced mid-frequency polarisation arc among the tested chemistries under the present measurement conditions. In long-term cycling, the NFM cells exhibit the fastest capacity fade and the strongest EIS impedance increase among the tested Na-ion chemistries, accompanied by more pronounced evolution of ICA/DVA features. By contrast, NFPP remains comparatively stable over extended cycling within the tested windows, indicating that the NFM chemistry is more sensitive to resistance increase and ageing under the applied protocols.

### 4.2. Implications for operability limits, state estimation and monitoring

The temperature-dependent characterisation, together with the NFM population statistics and cross-chemistry benchmarks, allows operating-condition effects to be distinguished from cell-to-cell variability in forms that are directly usable for pack-level control. For charging supervision, the NFM population results at low temperature (0 °C) show that a uniform voltage-based termination does not ensure uniform charge throughput once the cell kinetics are becoming the limiting factor. The charging-duration distribution develops a pronounced right tail that is dominated by the CV phase, whereas durations remain tightly clustered at 25 °C and 45 °C. As a result, fixed voltage thresholds can drive SOC imbalance and non-uniform heat generation at pack level. Mitigation should therefore rely on dispersion-aware constraints that are measurable in operation, including CV-duration statistics and pulse-relevant resistance within the intended SOC window. This probabilistic treatment is consistent with recent studies on commercial Na-ion cells, where high-SOC complications such as leakage currents, self-discharge, and cold-charge sensitivity can bias balancing logic and SOH inference when treated as deterministic or chemistry-invariant [7,9,11,54].

For power capability assessment, definitions should be tied to control-relevant pulse durations rather than to frequency-domain impedance. The pulse-response comparison shows that separating the initial IR (ohmic) drop from the subsequent polarisation voltage during the pulse is chemistry dependent, which determines the available voltage headroom for a given pulse duration. The mismatch between pulse-based DCR and EIS-derived resistance under low-temperature operation further indicates that RC polarisation dominates on the 1 s to 10 s time scale. Power capability calibration should therefore use transient metrics extracted for the intended pulse duration, while EIS remains valuable for mechanistic diagnosis and periodic parameter tracking rather than a direct measure of DC power capability.

For state estimation, OCV characterisation shows that OCV hysteresis, curve-shape change and cell-to-cell variability are inherently temperature specific and chemistry specific. Under the applied relaxation protocol, NFM exhibits negligible hysteresis beyond mid-SOC at

25 °C to 45 °C, whereas significant charge–discharge separation and low-SOC shape distortion emerge at 0 °C. The larger cell-to-cell variability and stronger temperature sensitivity observed in CFM necessitate explicit uncertainty quantification for OCV-based estimation. Conversely, NFPP maintains high consistency within a distinct mid-SOC window, with OCV-based SOC estimation becoming less reliable outside this region. These behaviours require OCV maps indexed by temperature and tailored to chemistry, together with hysteresis models and estimators that propagate measured OCV variability into SOC confidence bounds. Where external parameterisation is employed, for example using half-cell data, transferability artefacts induced by counter-electrode instability can require explicit treatment in the estimator and in model calibration [8].

Beyond standard electrical measurements, the sensing and ageing results show that auxiliary signals can be useful, depending on chemistry and on the mechanical coupling achieved by the sensor mounting. Under the casing-mounted circumferential configuration, layered-oxide cells produce a robust casing-strain response that is aligned with voltage across 0 °C to 45 °C, and $d\varepsilon/dV$ features align with dQ/dV transitions. This supports the use of strain as an independent constraint for calibration and anomaly detection. The lack of a repeatable casing-strain signature in NFPP indicates that mechanical observability is not universal. Over service life, cumulative irreversible strain evolves alongside capacity fade and EIS impedance growth, which makes it a candidate SOH indicator when thermal compensation is implemented. The distinct degradation trajectories, with accelerated capacity fade in NFM and higher stability in NFPP, further support chemistry-specific ageing models. Mechanistic interpretation of differential-feature evolution remains tentative without electrode-resolved diagnostics, but the consistent trends across voltage profiles, differential analyses and EIS impedance growth provide practical indicators for onboard monitoring.

## 5. Conclusion

This work presents a comprehensive characterisation of commercial 18650 sodium-ion cells for monitoring, control, and model parameterisation. The study combines (i) population-scale statistics for a layered-oxide NFM chemistry and (ii) benchmarking measurements across additional chemistries (CFM, NFPP, LFP, and NCA) under aligned protocols. This approach enables cross-chemistry comparisons on a common experimental basis.

For the NFM population, the results delineate operability and observability boundaries relevant to system integration. Under cold operation, NFM shows increased performance loss and cell-to-cell variability under fixed voltage thresholds. Pulse-based DCR and EIS-derived impedance provide complementary information that is not interchangeable for defining power limits, and cold conditions amplify the divergence between these metrics. NFM also displays measurable OCV hysteresis and curve-shape distortion at 0 °C, contrasting with its higher-temperature repeatability. Comparative benchmarking under aligned protocols places these attributes in a broader cross-chemistry context. The Na-ion chemistries retain measurable capacity at −40 °C under the applied protocol, whereas the Li-ion reference cells do not sustain discharge. Regarding observability and ageing, casing strain provides a robust state indicator for layered-oxide cells (NFM and CFM) under the present mounting configuration, whereas no resolved casing-level signature is observed for the NFPP cell. For NFM, this mechanical signature co-evolves with accelerated capacity fade, providing a diagnostic signal that is not resolved for the tested NFPP cell under the present configuration.

These results underscore the need for chemistry-specific parameterisation and algorithmic adaptations that (i) define operating limits indexed by temperature and SOC using pulse-relevant resistance on the 1 s to 10 s time scale, (ii) adopt chemistry-specific OCV maps with explicit low-temperature hysteresis modelling and uncertainty quantification, and (iii) treat strain-based observability as chemistry dependent and configuration dependent rather than universal. Future work should extend this cell-level parameterisation to module-level and pack-level validation. This includes quantifying how thermal gradients and series-connected ageing heterogeneity interact with the identified cell-level constraints.

## CRediT authorship contribution statement

**Shiyun Liu:** Writing – original draft, Visualization, Methodology, Investigation, Conceptualization. **Kang Li:** Writing – review & editing, Supervision, Methodology, Conceptualization. **James Yu:** Investigation, Conceptualization. **Kailong Liu:** Investigation, Conceptualization.

## Declaration of competing interest

The authors declare that they have no known competing financial interests or personal relationships that could have appeared to influence the work reported in this paper.

## Acknowledgments

This work is partially supported by the Ofgem SIF funded project ‘Flexible Railway Energy Hubs’ (Project Ref: 10117383) and the EPSRC funded project ‘Networked Energy Hubs for Accelerating Decarbonization of Transport and Energy Sectors’ (Project Ref: UKRI 779). Shiyun Liu would like to thank the University of Leeds and SP Energy Networks for sponsoring his research.

## Appendix A. Supplementary data

Supplementary data for this article can be found online at doi:10.1016/j.apenergy.2026.127687.

## Data availability

Data will be made available on request.

## References

[1] Xu C, Behrens P, Gasper P, Smith K, Hu M, Tukker A, Steubing B. Electric vehicle batteries alone could satisfy short-term grid storage demand by as early as 2030. Nat Commun 2023;14(1):119.
[2] Yao A, Benson SM, Chueh WC. Critically assessing sodium-ion technology roadmaps and scenarios for techno-economic competitiveness against lithium-ion batteries. Nature Energy 2025;10(3):404–16.
[3] Rudola A, Sayers R, Wright CJ, Barker J. Opportunities for moderate-range electric vehicles using sustainable sodium-ion batteries. Nature Energy 2023;8(3):215–8.
[4] Vaalma C, Buchholz D, Weil M, Passerini S. A cost and resource analysis of sodium-ion batteries. Nat Rev Mater 2018;3(4):1–11.
[5] Abdolrasol MGM, Ansari S, Sarker IA, Tiong SK, Hannan MA. Lithium-ion to sodium-ion batteries transitioning: trends, analysis and innovative technologies prospects in EV application. Progress in Energy 2025;7(2):022007.
[6] Laufen H, Klick S, Ditler H, Quade KL, Mikitisin A, Blömeke A, Schütte M, Wasylowski D, Sonnet M, Henrich L, et al. Multi-method characterization of a commercial 1.2 ah sodium-ion battery cell indicates drop-in potential. Cell Rep Phys Sci 2024;5(5).
[7] Rehm M, Fischer M, Gomez MR, Schütte M, Sauer DU, Jossen A. Comparing the electrical performance of commercial sodium-ion and lithium-iron-phosphate batteries. J Power Sources 2025;633:236290.
[8] Schütte M, Laufen H, Luder D, Ditler H, Kern J, Klick S, Junker M, Stahl G, Frie F, Sauer DU. First full cell parameterization of a commercial layered oxide/hard carbon sodium-ion 18650 battery cell for a physico-chemical model. J Energy Storage 2025;107:114931.
[9] Dorau FA, Sommer A, Koloch J, Röß-Ohlenroth R, Schreiber M, Neuner M, Gamra KA, Lin Y, Schoberl J, Bilfinger P, et al. Comprehensive analysis of commercial sodium-ion batteries: structural and electrochemical insights. J Electrochem Soc 2024;171(9):090521.
[10] Jin B, Qiao D, Gao W, Yao S, Liu J, Zhu Z, Shao Y, Li D, Zheng Y. Low-temperature sodium dendrite-induced short circuit diagnosis for sodium battery. J Energy Storage 2025;111:115359.
[11] Streck L, Roth T, Bosch H, Kirst C, Rehm M, Keil P, Jossen A. Self-discharge and calendar aging behavior of li-ion and na-ion cells. J Electrochem Soc 2024;171(8):080531.
[12] Gao X, Bao Z, Zhang L, Brandon NP, Offer GJ, Wang H. Seeing the unseen: real-time tracking of battery cycling-to-failure via surface strain. Joule 2026;102272.
[13] Deng Z, Xu L, Liu H, Hu X, Duan Z, Xu Y. Prognostics of battery capacity based on charging data and data-driven methods for on-road vehicles. Appl Energy 2023;339:120954.

[14] Figgener J, van Ouwerkerk J, Haberschusz D, Bors J, Woerner P, Mennekes M, Hildenbrand F, Hecht C, Kairies K-P, Wessels O, et al. Multi-year field measurements of home storage systems and their use in capacity estimation. Nature Energy 2024;9(11):1438–47.
[15] Naguib M, Chen J, Kollmeyer P, Emadi A. Thermal fault detection of lithium-ion battery packs through an integrated Physics and deep neural network based model. Communications Engineering 2025;4(1):1–9.
[16] Torres-Castro L, Lamb J. United States Advanced Battery Consortium battery abuse testing manual for electric and hybrid vehicle applications. Technical report, Sandia National Lab.(SNL-NM), Albuquerque, NM (United States); United States; 2022.
[17] Lin S, Zhang H, Shu C, Hua W, Wang X, Zhao Y, Luo J, Tang Z, Wu Y, Tang W. Research progress and perspectives on pre-sodiation strategies for sodium-ion batteries. Adv Funct Mater 2024;34(51):2409628.
[18] Standard IEC. 62660-1. Secondary lithium-ion cells for the propulsion of electric road vehicles—part 1: performance testing. Switzerland: International Electrotechnical Commission: Geneva; 2010.
[19] Barai A, Uddin K, Widanage WD, McGordon A, Jennings P. A study of the influence of measurement timescale on internal resistance characterisation methodologies for lithium-ion cells. Scientific Reports 2018;8(1):21.
[20] Liu S, Li K, Yu J. Battery pack condition monitoring and characteristic state estimation: challenges, techniques, and future prospectives. J Energy Storage 2025;105:114446.
[21] Naylor Marlow M, Chen J, Wu B. Degradation in parallel-connected lithium-ion battery packs under thermal gradients. Commun Eng 2024;3(1):2.
[22] Plank C, Rüther T, Jahn L, Schamel M, Schmidt JP, Ciucci F, Danzer MA. A review on the distribution of relaxation times analysis: a powerful tool for process identification of electrochemical systems. J Power Sources 2024;594:233845.
[23] Liu Z, Wang C, Guo X, Cheng S, Gao Y, Wang R, Sun Y, Yan P. Thermal characteristics of ultrahigh power density lithium-ion battery. J Power Sources 2021;506:230205.
[24] Fan C, Liu K, Zhu T, Peng Q. Understanding of lithium-ion battery degradation using multisine-based nonlinear characterization method. Energy 2024;290:130230.
[25] Barai A, Uddin K, Dubarry M, Somerville L, McGordon A, Jennings P, Bloom I. A comparison of methodologies for the non-invasive characterisation of commercial li-ion cells. Prog Energy Combust Sci 2019;72:1–31.
[26] Sun D, Yu X, Wang C, Zhang C, Huang R, Zhou Q, Amietszajew T, Bhagat R. State of charge estimation for lithium-ion battery based on an intelligent adaptive extended kalman filter with improved noise estimator. Energy 2021;214:119025.
[27] Zhang C, Li K, Deng J. Real-time estimation of battery internal temperature based on a simplified thermoelectric model. J Power Sources 2016;302:146–54.
[28] Zhang C, Amietszajew T, Li S, Marinescu M, Offer G, Wang C, Guo Y, Bhagat R. Real-time estimation of negative electrode potential and state of charge of lithium-ion battery based on a half-cell-level equivalent circuit model. J Energy Storage 2022;51:104362.
[29] Bharathraj S, Kaushik A, Adiga SP, Kolake SM, Song T, Sung Y. Accessing the current limits in lithium ION batteries: analysis of propensity for unexpected power loss as a function of depth of discharge, temperature and pulse duration. J Power Sources 2021;494:229723.
[30] Aitio A, Howey DA. Predicting battery end of life from solar off-grid system field data using machine learning. Joule 2021;5(12):3204–20.
[31] Geslin A, Xu L, Ganapathi D, Moy K, Chueh WC, Onori S. Dynamic cycling enhances battery lifetime. Nature Energy 2024:1–9.
[32] Jöst D, Palaniswamy LN, Quade KL, Sauer DU. Towards robust state estimation for lfp batteries: model-in-the-loop analysis with hysteresis modelling and perspectives for other chemistries. J Energy Storage 2024;92:112042.
[33] Tran M-K, DaCosta A, Mevawalla A, Panchal S, Fowler M. Comparative study of equivalent circuit models performance in four common lithium-ion batteries: lfp, NMC, lmo, NCA. Batteries 2021;7(3):51.
[34] Farmann A, Sauer DU. A study on the dependency of the open-circuit voltage on temperature and actual aging state of lithium-ion batteries. J Power Sources 2017;347:1–13.
[35] Liang X, Song X, Sun HH, Kim H, Kim M-C, Sun Y-K. High-energy and long-life o3-type layered cathode material for sodium-ion batteries. Nature Communications 2025;16(1):3505.
[36] Liu S, Li K, Yu J. Adaptive estimation of battery pack state of charge with optical fibre strain measurements. Appl Energy 2026;407:127330.
[37] Che C, Wu F, Li Y, Li Y, Li S, Wu C, Bai Y. Challenges and breakthroughs in enhancing temperature tolerance of sodium-ion batteries. Adv Mater 2024:2402291.
[38] Bai Z, Yao Q, Wang M, Meng W, Dou S, Liu HK, Wang N. Low-temperature sodium-ion batteries: challenges and progress. Adv Energy Mater 2024;14(17):2303788.
[39] Wang M, Yin L, Zheng M, Liu X, Yang C, Hu W, Xie J, Sun R, Han J, You Y, et al. Temperature-responsive solvation enabled by dipole-dipole interactions towards wide-temperature sodium-ion batteries. Nature Communications 2024;15(1):8866.
[40] Zhang J, Gai J, Song K, Chen W. Advances in electrode/electrolyte interphase for sodium-ion batteries from half cells to full cells. Cell Reports Physical Science 2022;3(5).
[41] Galeotti M, Cinà L, Giammanco C, Cordiner S, Di Carlo A. Performance analysis and SOH (state of health) evaluation of lithium polymer batteries through electrochemical impedance spectroscopy. Energy 2015;89:678–86.
[42] Westerhoff U, Kroker T, Kurbach K, Kurrat M. Electrochemical impedance spectroscopy based estimation of the state of charge of lithium-ion batteries. J Energy Storage 2016;8:244–56.
[43] Phogat P, Dey S, Wan M. Comprehensive review of sodium-ion batteries: principles, materials, performance, challenges, and future perspectives. Mater Sci Eng B 2025;312:117870.
[44] Mao J, Zhang P, Liu X, Liu Y, Shao G, Dai K. Entropy change characteristics of the lini0. 5mn1. 5o4 cathode material for lithium-ion batteries. ACS omega 2020;5(8):4109–14.
[45] Nejad S, Gladwin DT, Stone DA. A systematic review of lumped-parameter equivalent circuit models for real-time estimation of lithium-ion battery states. J Power Sources 2016;316:183–96.
[46] Özdogru B, Dykes H, Gregory D, Saurel D, Murugesan V, Casas-Cabanas M, Çapraz ÖÖ. Elucidating cycling rate-dependent electrochemical strains in sodium iron phosphate cathodes for na-ion batteries. J Power Sources 2021;507:230297.
[47] Xie Y, Gao H, Harder R, Li L, Gim J, Che H, Wang H, Ren Y, Zhang X, Li L, et al. Revealing the structural evolution and phase transformation of o3-type nani1/3fe1/3mn1/3o2 cathode material on sintering and cycling processes. ACS Appl Energy Mater 2020;3(7):6107–14.
[48] Wang C, Sun Z, Liu Y, Liu L, Yin X, Hou Q, Fan J, Yan J, Yuan R, Zheng M, et al. A weakly coordinating-intervention strategy for modulating na+ solvation sheathes and constructing robust interphase in sodium-metal batteries. Nature Communications 2024;15(1):6292.
[49] Wable M, Bal B, Capraz ÖÖ. Probing electrochemical strain generation in sodium chromium oxide (nacro 2) cathode in na-ion batteries during charge/discharge. Energy Adv 2024;3(3):601–8.
[50] Aktekin B, Riegger LM, Otto S-K, Fuchs T, Henss A, Janek J. SEI growth on lithium metal anodes in solid-state batteries quantified with coulometric titration time analysis. Nature Communications 2023;14(1):6946.
[51] Cui R, Ma Y, Gao X, Wang W, Wang J, Xing Z, Ju Z. Research progress of co-intercalation mechanism electrolytes in sodium-ion batteries. Energy Storage Mater 2024:103627.
[52] Forero-Saboya J, Desai P, Corominas RH, Raymundo-Piñero E, Canizarès A, Foix D, Tarascon J-M, Mariyappan S. Influence of formation temperature on cycling stability of sodium-ion cells: a case study of na3v2 (po4) 2f3| HC cells. J Electrochem Soc 2023;170(10):100529.
[53] Dubarry M, Anseán D. Best practices for incremental capacity analysis. Frontiers in Energy Research 2022;10:1023555.
[54] Bischof K, Feinauer M, Regalado AA, Wohlfahrt-Mehrens M, Hölzle M, Waldmann T. Sodium metal deposition in commercial sodium-ion cells. J Electrochem Soc 2025;172(9):090520.